DOUBLE CHARGE EXCHANGE OF PIONS ON HELIUM-4

thesis by

Jeffrey Eugene Ungar

In Partial Fulfillment of the Requirements
For the Degree of
Doctor of Philosophy

California Institute of Technology
Pasadena, California
1983

(Submitted: December 15, 1982)

ACKNOWLEDGEMENTS

I would like to express my sincere gratitude to the staff, faculty and students of the Kellogg Radiation Laboratory for making my four and a half years here both pleasurable and scientifically stimulating. In particular, I would like to thank my advisor, Robert D. McKeown, for his boundless patience and enthusiasm in his roles both as teacher and collaborator. In addition to Bob, I would like to thank the other collaborators on Experiment 564, namely Don Geesaman, Roy Holt, Chris Morris, Jim Specht, Ken Stephenson, and Ben Zeidman, all of whom worked very hard to make this experiment a success. I am deeply indebted to Professors Charles Barnes, Ralph Kavanagh, Steven Koonin, Thomas Tombrello, and Ward Whaling, for their countless useful suggestions and helpful conversations. Wil Schick, Bob Stevens, and Don Woshnak of our machine shop each deserve medals for their heroic efforts at turning crudely penciled sketches into finished pieces of apparatus in record time, as does Al Massey for his skill at keeping our countless pieces of electronics in working order. The superbly competent engineering support provided by the LAMPF staff, and in particular our project engineer, Gil Suazo, is gratefully acknowledged.

Many thanks are due the National Science Foundation for its support from 1978 through 1981 under its Graduate Fellowship program, as well as the Gulf Oil Corporation for naming me a Graduate Fellow during the year 1982.

Finally, and most importantly, I would like to thank my parents and brothers. Without their love and encouragement I could never have completed this work.

This research was supported in part by the National Science Foundation under Grant No. PHY79-23638.

ABSTRACT

The reaction $^4He(\pi^-,\pi^+)4n$ at an incident π^- energy of 165 Mev has been measured at 0° in a search for bound states of the tetraneutron and resonant states in the continuum. No resonant structure was observed, and a cross section of 7 ± 15 nb/sr has been determined for bound tetraneutron production by this reaction. The measured cross section magnitudes are consistent with the related measurements of Falomkin *et al* and Stetz *et al*, but are larger than the results of Kaufman *et al* and the calculations of Gibbs *et al* by a factor of at least 100. The relevance of these results to identification of the pion double charge exchange reaction mechanism is discussed.

TABLE OF CONTENTS

I. General Introduction

With the advent of the "meson factory" accelerator facility within the last decade, capable of providing pion and muon beams of high intensity, uniformity, and reproducibility, exotic reactions between these particles and the atomic nucleus have become amenable to experimental investigation. The pion, in particular, is a unique probe of the nucleus because of its role as the mediator of the long range part of the nuclear force, and as such, its interactions are radically different from those of other particles such as electrons, photons, and nucleons. Its bosonic nature leads to the possibility of such reactions as pion absorption and photoproduction, as well as conventional elastic and inelastic scattering. The point of investigating these processes, their own intrinsic interest aside, is the hope that their study will provide information about nuclear structure that is complementary to that available from the more familiar reactions.

An unusually interesting class of reactions which the pion opens to the experimenter is that of charge exchange. The pion, which comes in three charge states, π^+,π^0,and π^-, can undergo interactions with the proton and neutron in which the pion changes its charge by a single unit, with the nucleon changing its charge by the opposite amount. The uniqueness of the pion lies in the fact that it can perform this feat *twice*, going from a π^- to a π^+, having turned two protons into neutrons in the process, and conversely, a π^+ going to π^- can transform two neutrons into two protons. This property opens the possibility of taking existing nuclei and creating new ones very neutron rich or very proton rich, which may be difficult or impossible to investigate in any other fashion.

A particularly interesting nucleus, the existence or nonexistence of which has been the subject of investigations for over a decade and a half, is the tetraneutron, a bound nucleus consisting entirely of neutrons. Other than the trivial case of the lone neutron, there are no known examples of nuclei without protons, although at various points in history the ^{2}n, the ^{3}n, and the ^{6}n have been searched for, all without success. In spite of the failure of searches for the trineutron, and the current firm belief in the nonexistence of the bound dineutron, considerations of nuclear binding systematics indicate that the tetraneutron could be expected to be more tightly bound than either of the above nuclei, and might in fact be stable against decay by particle emission, although it would, of course β decay to ^{4}H. Proof of its existence would be a very exciting development.

Yet another motivation for carrying out double charge exchange (DCX) experiments is the belief that this process, which by its nature must involve two nucleons, can act as a probe of nucleon-nucleon correlations inside the nucleus, as opposed to single step processes, which are sensitive (in first order, at least) only to one-nucleon matrix elements. Experiments involving DCX are as yet limited in number, and new reactions are being eagerly investigated.

II. Status of the Tetraneutron

A. Calculations of 4 Neutron Binding

The four body problem in nuclear physics is a particularly difficult one, with neither few enough particles (three) to be treated with the standard Faddeev equation techniques, nor many enough for the mean field assumptions that underly the shell model to be obviously valid. Nevertheless, approximate calculations have been attempted in the search for possible bound states and resonances of the 4 neutron system.

Tang and Bayman (Ta65) have attempted to resolve the question of binding in the four neutron system by a variational calculation. Their trial wave function was taken to consist of a pair of spin-singlet dineutrons (with identical internal wave functions) in a relative s state, with seven free parameters describing the internal and relative wave functions, a simplified hard core neutron-neutron interaction fitted to the low energy p-p $^1S_0$ scattering data (corrected for Coulomb effects) being used in the model Hamiltonian. For values of the other parameters which minimized the Hamiltonian, the energy proved to be a monotonically decreasing function of the separation of the dineutron clusters, indicating that neither a bound state nor a resonance was formed. Several other neutron-neutron potentials were tried, but no qualitative change in the results was found.

Thompson (Th70) has performed a resonating group calculation which made similar assumptions about the functional form of the 4 neutron state vector system, and similarly found no evidence for binding. This result should be compared to the gcod agreement obtained by similar methods, with the experimental binding energies of ^3H and ^3He.

The assumptions that underly the previous variational calculations are difficult to justify rigorously, and of course any variational calculation can only provide an upper bound on the ground state energy of a system. A more systematic approach to the problem is provided by the K-harmonic formalism of Siminov (Si66) as applied to the four nucleon system by Badalyan *et al* (Ba68b), in which the true wave function is expanded in a series of eigenfunctions of an operator which is the higher dimensional analog of angular momentum. As is the case for the variational calculations, only an upper bound can be placed on the ground state energy. Several different simplified forms for the potential were taken, all of them failing to produce binding of the 4-neutron complex.

B. Experimental Evidence

Observation of the beta decay of ^{8}He implies its stability with respect to the particle decay $^{8}\text{He} \rightarrow {}^{4}\text{He} + {}^{4}\text{n}$, setting an upper limit to the binding of the ^{4}n (Me68). The currently accepted value for the mass of the ^{8}He nucleus limits the binding energy of the ^{4}n to 3.1 Mev or less. If, within these limits, the tetraneutron actually exists, its T=2 isobaric partners should be found in the other four nucleon systems, with calculable energy differences due to electromagnetic effects. The calculated T=2 analog state in ^{4}He, for example, should be found between 26 and 29 Mev excitation (Fi73). No such states have yet been unambiguously identified. An early assignment of T=2 to a level in ^{4}H (Ar63) has not been confirmed, and in fact would imply (Sc63) a tetraneutron binding of $\approx$ 4.5 Mev, in contradiction to the observed stability of ^{8}He as discussed above.

Schiffer and Vandenbosch (Sc63) conducted a search for tetraneutrons produced in the thermal neutron fission of ^{235}U, arguing that the

abundance of tetraneutrons (if they exist) produced should be comparable to those of alphas, tritons, and protons because of the absence of the Coulomb barrier. Aluminum and nitrogenous targets were irradiated in reactors, and radioactivity from the products of the reactions $^{27}Al(^{4}n,^{3}H)^{28}Mg$, $^{27}Al(^{4}n,p2n)^{28}Mg$, and $^{14}N(^{4}n,n)^{17}N$ was searched for. With cross sections for these reactions estimated from those for (α,n) and (α,p) on neighboring light nuclei, the production of tetraneutrons in thermal fission was determined to be $\leq 10^{-4}$ than that of alphas, or less than 4 tetraneutrons per 10^{7} fissions.

Observing that the production of alphas and tritons is far higher in fast deuteron induced fission than in thermal neutron fission, Cierjacks *et al* (Ci65) bombarded natural uranium with 50 Mev deuterons, and similarly looked for tetraneutron induced activity in a variety of targets. The most sensitive test was for induced activity in ^{209}Bi through the reaction $^{209}Bi(^{4}n,n)^{212}Bi$, and a limit of one tetraneutron per 5×10^{9} fast fissions was concluded.

Sun *et al* (Su52) looked at the reactions $^{103}Rh(n,^{4}n)^{100}Rh$ and $^{209}Bi(n,^{4}n)^{206}Bi$ by bombarding the targets with neutrons at energies below the thresholds for production of free neutrons in the final state, and monitored the radioactivity of the heavy product nuclei. They were able to set cross section upper limits of several microbarns for production of tetraneutrons bound by more than 3 Mev, although the ^{8}He stability indicates that the tetraneutron must be bound by less than this, and hence their failure to detect tetraneutrons is to be expected.

Brill *et al* (Br64) investigated the reactions $^{48}Ca(^{3}He,^{4}n)^{47}Ti$ and $^{48}Ca(^{12}C,^{4}n)^{56}Fe$ by measuring the time of flight versus pulse height of final state neutron clusters with hydrogenous scintillators. No indication

of tetraneutrons production was found, with a cross section limit of 4 μb established for the latter reaction, and 6 μb for the former.

Cerny *et al* (Ce74) searched for tetraneutrons produced in the reaction $^{7}Li(^{7}Li,^{10}C)^{4}n$ at a bombarding energy of 79.6 Mev by looking at the energy spectrum of the product ^{10}C. An upper limit of 30 nb/sr was set on production of ^{4}n at 7.4°.

Cohen *et al* (Co65) looked at the energy spectrum of ^{3}He nuclei produced in the reaction $^{7}Li(\pi^{-},^{3}He)^{4}n$ in a search for both bound and unbound 4 neutron complexes. No peak was found in the zero binding region, and an upper limit of one tetraneutron producing reaction per 2000 pion capture reactions was set, a limit not sufficiently stringent to exclude the existence of the tetraneutron when compared to the corresponding ratio for production of ^{4}H (Fi73) in pion capture on ^{7}Li.

Arnaldi *et al* (64) measured the radioactivity induced in aluminum by the reaction $^{27}Al(^{4}n,2n)^{29}Al$ where the tetraneutrons were to be generated by the reaction $^{4}He(\gamma,2\pi^{+})^{4}n$, the gammas ranging up to an energy of 1 Gev. The results of the experiment were negative, with a limit of 1.7 μb set on tetraneutron production.

All of the latter searches have attempted to produce tetraneutrons through reactions that proceed through highly excited intermediate states, conditions under which one might reasonably expect production of weakly bound systems to be suppressed. The reaction $^{4}He(\pi^{-},\pi^{+})^{4}n$, because of the possibility of low momentum transfer, would seem to offer the best hope of creation of an unexcited tetraneutron. Davis *et al* (Da64b) first investigated this reaction at T_{π^-} = 105 and 165 Mev, at 90° in the lab frame, observing the momentum spectrum of the π^{+}. A limit of 1μb/ sr for bound or resonant states at both energies was established.

Gilly *et al* (Gi65) performed an experiment in which the incident π^- energy was varied from 170 to 215 Mev in 6 Mev steps, while the π^+ were observed at the fixed energy of 176 Mev, this search covering the tetraneutron binding energy range of between -20 and +10 Mev. A limit of 200 nb/sr at 0° was placed on this reaction, a result which seemed at the time to be quite stringent. More recent investigations of double charge exchange reactions to discrete nuclear final states have shown that these cross sections are often of this order of magnitude or even smaller, and that higher sensitivity and energy resolution is necessary for conclusive results.

Kaufman *et al* (Ka67,68) investigated this reaction for T_{π^-}=140Mev, observing the π^+ energy spectrum at 20° (lab) with 1 Mev energy resolution. They quote an upper limit of 0.14nb/sr for tetraneutron production in this reaction for binding energies between -10 and +10 Mev, which would seem to be quite conclusive. Unfortunately, the double charge exchange calculations of Becker and Schmit (Be70) which are in good agreement with the measurement of Gilly *et al*, give results a factor of 2300 too large for consistency with Kaufman *et al*, leading to suspicions that this measurement might be in error. Stetz *et al* (St81) have measured $^4He(\pi^+,\pi^-)4p$ under kinematic conditions identical to those of Kaufman, and have found continuum differential cross section larger by a factor of 100. It appears, therefore, that the limits arrived at in the Kaufman *et al* experiment cannot be viewed as being in any way conclusive, leaving the question of existence of the tetraneutron very much open.

III. Theories of DCX and Comparison with Experiment

A. Cascade Model

The simplest possible mechanism for double charge exchange on a nucleus involves two successive stages of single charge exchange, proceeding by way of an intermediate state of the system consisting of a π^0 and a nucleus with one more (or less) positive charge than the initial one. This model is known as the cascade process. One may crudely estimate the expected order of magnitude for the ^{4}He DCX cross section that will result from this process by a simple geometric argument. Since there is a single pair of protons available, the cross section for the pion undergoing a single charge exchange is roughly twice that for an elementary pion-nucleon single charge exchange. The probability of the resulting π^0 undergoing another single charge exchange to π^+ is the pion-nucleon charge exchange cross section divided by $4\pi r_{av}^2$ (r_{av} being defined as the root-mean-square separation between protons). At the 3,3 resonance the pion-nucleon charge exchange cross section is roughly 50 mb, and one may estimate the r.m.s. nucleon separation as 2.8 fermis. The resulting estimate for ^{4}He(π^-,π^+)4n comes to 5 mb. The measured DCX total cross section on resonance for ^{4}He(π^+,π^-)4p (which should be comparable to ^{4}He(π^-,π^+)4n by isospin invariance) is roughly .3 mb, more than an order of magnitude smaller than this estimate. This is not at all surprising, when one considers that we have neglected the effects of nucleon Fermi motion, which will tend to wash out the effect of the resonance, have ignored the Pauli suppression of the reaction at low momentum transfer, and have failed to consider the effect of "shadowing" of nucleons by each other, as well as competition from other strong reaction channels, most

importantly pion absorption. A similar classical analysis of DCX has been given by Becker and Batusov (Be71) as well as by Noak(No71).

Quantum mechanically, the cascade assumption is equivalent to adopting the impulse approximation (*i.e.*, taking the pion-nucleon transition element to be unaffected by the nuclear medium) and including only *one* intermediate nuclear state in the calculation. It can be shown (Be71) that these calculations are independent of the two body correlations in the nuclear wave functions. Such calculations have been carried out by Batusov *et al* (Ba68b) using Monte Carlo methods.

B. Pair Mechanism

A more realistic calculation invoking closure but still based on the sequential single-charge exchange mechanism (see figure 1a) takes into account the amplitude due to off-shell π^0 propagation between charge exchanges, which requires knowledge of the pion scattered wave function at finite distances from the scatterer (in this case a proton), information unavailable from free pion-nucleon scattering, which samples only asymptotic behavior. The off shell t-matrix must then be guessed at using either some elementary particle theory or by extraction from experiments which sample the short range behavior of the wave function. This point of view pictures the DCX as taking place on a correlated pair of nucleons and will be sensitive to the two nucleon correlation function of the nuclear states.

An early calculation of this sort was that of Parsons *et al* (Pa65) who calculated the cross section for $^3He(\pi^-,\pi^+)3n$ in the impulse approximation using the Chew-Low theory of pion-nucleon interactions to derive the off-shell behavior required. A later calculation of $^4He(\pi^-,\pi^+)4n$ was

carried out by Becker and Schmit (Be70) with the off-shell behavior of the pion-nucleon vertex calculated by way of dispersion relations under the assumption of dominance of the amplitude by the 3,3 resonance, with an approximate treatment of the final state phase space integral. More recently, a treatment of $^4He(\pi^+,\pi^-)4p$ incorporating the full effects of the Pauli principle, exact treatment of the phase space, and nucleon spin flip amplitudes was reported. In this work, due to Gibbs et al (Gi77), the off-shell behavior was modeled by a simple analytic extrapolation of the on-shell transition amplitudes, the parameters of which were fitted to pion-deuteron absorption. None of these microscopic calculations take pion absorption into account.

C. Exotic Mechanisms

An alternative mechanism for DCX was proposed by Dalkarov and Shapiro (Da64a) and is represented by the Feynman diagram of figure 1b. In this process, which because of the energy dependence of the relevant vertices might be expected to dominate at higher energies ($\geq$1Gev) than the previous mechanism, the pion charge exchange takes place in one step instead of two, creating a Δ^- isobar in the residual nucleus, which then interacts with the surviving proton to create two neutrons. If one considers only vertices which involve three particles to be "elementary", one sees that the aforementioned interaction can be represented by the Feynman diagram of figure 1c, which has been proposed by Brown *et al* (Br82) in connection with pion absorption.

Germond and Wilkin (Ge75,79) have done a calculation of $^4He(\pi^+,\pi^-)4p$ adopting the mechanism of diagram d of figure 1, in which the incoming pion scatters a virtual pion of opposite charge in the

"cloud" surrounding the target nucleon out of the nucleus, and is itself absorbed on another nucleon. It should be emphasized that (in the region of the 3,3 resonance, at least) this mechanism is identical with the previous one, the difference lying only in whether one considers the isobar to be an independent elementary particle, or merely a state of the pion-nucleon system. This calculation, which was meant only to provide an order of magnitude estimate of the contribution of such a mechanism, ignores complications such as wave function asymmetry (Pauli principle) and full phase space. It adopts the ordinary Feynman rules of relativistic perturbation theory, with a simple first order $\bar{u}\gamma_5 u$ pion nucleon vertex (without a form factor), and a π^-–π^+ scattering amplitude taken from PCAC current algebra soft pion theorems and assumed valid for physical pions as well.

D. Comparison with Previous Experiments

The angular distributions generated by the cascade model, which predict strong peaks in the backward hemisphere, are in sharp contrast to the experimental results, which show little or no deviation from a purely phase space distribution, indicating isotropy in the center of mass frame. For this reason, the cascade model has been largely abandoned in favor of more sophisticated treatments.

Figure 2, (from Stetz *et al*, St81) shows experimental total cross sections for ^{4}He(π^+,π^-)4p displayed against the predictions of Becker and Schmit, Gibbs *et al*, and Germond and Wilkins. Surprisingly, the Gibbs *et al* results are smaller than those of Becker and Schmit by a factor of 2300 in the resonance region, although both use the same mechanism. The discrepancy between the two calculations has been ascribed by the

former group to their improved treatment of the off-shell pion-nucleon transition amplitude and more accurate phase space integrals. With a difference of more than three orders of magnitude while invoking identical mechanisms, it seems hard to believe that an error has not crept into one or another of these calculations. The original Kaufman *et al* measurement (Ka67,68) of $^4He(\pi^-,\pi^+)^4n$ at 20° (in the lab frame) which was well reproduced by the Gibbs calculation and cited by the latter as confirmation of their accuracy has since been shown to conflict directly with several other mutually consistent determinations giving results larger by a factor of 100, and seems likely to have been erroneous. Similarly, Gibbs *et al* underpredict the cross sections of Falomkin *et al* (Fa74,76) as well as Stetz *et al* (St81) by between one and two orders of magnitude. In contrast to this failure, Becker and Schmit reproduce the 0° data of Gilly *et al* (Gi65) quite well, although they do seem to overpredict the total cross sections near resonance as measured by Falomkin *et al*. Although the Germond and Wilkins model seems to be in fair agreement with the total cross section data as well as with the poor statistics data of Carayannopoulos *et al* (Ca68) at 485 Mev, many of the assumptions of the model seem very difficult to justify. For instance, the Pauli principle, which they neglect entirely, would certainly reduce the cross section substantially (near resonance, Gibbs *et al* show suppression by a factor of 2 due to Pauli effects alone). Neither is it clear that the use of soft pion transition elements and unrenormalized pion nucleon vertices are appropriate. It seems, therefore, that a realistic estimate of the contribution of this mechanism awaits more sophisticated calculations.

It should be pointed out that there is a certain amount of evidence pointing to the essential correctness of the pair mechanism of DCX, at

least at high momentum transfers in heavier nuclei. Schiffer (Sc80) has compared the energy spectrum of 240 Mev π^+ inelastically scattered on ^{16}O as measured at 60° to a single scattering impulse approximation calculation, finding excellent agreement except at the low energy end of the spectrum, where the calculation goes to zero much faster than shown by the measurement. If one ascribes the inelastic π^+ in this region to be due to double scattering alone, and takes the DCX mechanism to be due primarily to the pair process, the DCX spectrum should equal the two step inelastic contribution (multiplied by appropriate isospin factors). Adding the $^{16}O(\pi^+,\pi^-)^{16}Ne$ (240 Mev, 50°) spectrum multiplied by 17 (the actual isospin arithmetic predicts a factor of 19.75) to the aforementioned calculation for single step inelastic scattering, Schiffer reproduces the experimental spectrum very nicely.

At high energies, above 1 Gev, it is clear that the simple pair mechanism no longer dominates, as the single charge exchange cross section for pions on nucleons rapidly approaches zero with increasing energy in this region. Indeed, the measured DCX cross section for $^4He(\pi^+,\pi^-)4p$ at 1.7 Gev is larger than the abovementioned "naive" estimate based on sequential single charge exchange by a factor of 50 (Je80). In the same energy region, however, the pion production cross section is rising rapidly, and it is reasonable to expect that a mechanism in which one of the resulting pions is emitted while another one of them is absorbed on a neighboring nucleon might predominate. This mechanism is essentially identical to those of Germond *et al* and Dalkarov *et al*.

Cooper (Co79) and Seth (Se79) have reviewed the experimental results of DCX to discrete states in heavier nuclei, and more recently, Greene *et al* (Gr82) have presented results of a similar nature. Angular

distributions of many of these reactions show minima seemingly diffractive in nature, but corresponding to nuclear radii far too large to be reconciled with those derived from electron scattering measurements. Working within the framework of an optical model of charge exchange scattering (see also Jo80 and Sp78 for this approach), M. B. Johnson and E. R. Siciliano (as quoted by Gr82) find it possible to accurately fit the measured angular distributions by adding an isotensor term in the optical potential quadratic in the nuclear density. This sort of behavior is indicative of a two step mechanism, and provides further evidence in favor of the pair model. It seems, therefore, in spite of the disagreement between the calculation of Gibbs *et al* and experiment, a conclusion that mechanisms other than the pair process need to be invoked to explain DCX in the several hundred Mev range is premature. An investigation into the cause of the discrepancies between the calculations of Becker and Schmit and those of Gibbs *et al* promises to shed much light on the true contribution of the pair mechanism to DCX.

IV. The Present Experiment

In view of the inconclusive nature of the previous attempts at creation and detection of the tetraneutron, a more sensitive search using the $^4He(\pi^-,\pi^+)^4n$ reaction seemed warranted. The arrangement of Gilly et al (Gi65), in which the energy of the incident π^- was varied while that of the detected π^+ remained fixed was less suitable than the converse setup, because of the difficulty in sorting out the effects of the energy variation of the underlying DCX mechanism cross section from those due to nuclear structure, the primary object of interest. The Δ resonance of the elementary pion-nucleon interaction near 160 Mev indicated that the overall DCX cross section might be expected to peak at or near that energy, and so T_{π^-} was fixed at 165 Mev. Recent measurements (e.g., Gr82) of DCX to discrete states have since shown that these cross sections do not necessarily show such behavior.

Elementary nuclear shell model considerations indicate that the ground state of the bound tetraneutron would have a spin-parity assignment of 0^+, with a pair of neutrons in the $1s_{1/2}$ subshell, and another pair coupled to zero total angular momentum in the $1p_{3/2}$ subshell. The ^4He nucleus also has $J^\pi=0^+$, and one would therefore expect a forward peaking of the ground state-ground state transition. More importantly, the expected small magnitude of the residual nucleus' binding energy makes its production difficult in a reaction imparting significant momentum to the target, as a breakup would be far more likely. Becker and Batusov (Be71) have compared the experimental results for 195 Mev π^+ DCX on ^7Li at 0° and at 15° and show that while the 0° π^- spectrum shows a very prominent peak corresponding to transitions to bound states, the other

spectrum shows no peaking whatsoever. Similarly, Greene *et al* (Gr82) have found strong angular dependences in DCX to discrete states. It was therefore deemed desirable to run at angles as small as practical, and it proved possible in practice to run at 0°.

V. Experimental Apparatus

A. General Layout

The overall experimental layout is diagrammed in figure 3. A beam of π^- bombards a liquid ^{4}He target, most of them being transmitted with only slight loss of energy, a small fraction undergoing $^4\mathrm{He}(\pi^-,\pi^+)4\mathrm{n}$. Upon leaving the target region, the particles enter the field of a dipole magnet, and are selected according to charge. Negative particles, primarily unreacted π^- from the beam, are deflected to the left, away from the remainder of the analysis system, while those of positive charge, including the π^+ of interest, are directed to the right, into the magnetic spectrometer.

In the spectrometer, the particles are magnetically bent upwards, the curvature of the path being inversely proportional to momentum. Measurement of the position of each particle at four points along the trajectory enables reconstruction of the entire trajectory, and, in particular, calculation of the particle's momentum. At the focal plane of the spectrometer, a Cerenkov counter, which detects only those charged particles moving above a certain threshold velocity, irrespective of their mass, is used to discriminate between π^+ and contaminant particles. The data are sent to the data acquisition computer on an event by event basis, and are stored on magnetic tape for later analysis.

The apparatus will now be described in detail.

B. The Beam Line

The experiment was run on the Pion Particle Physics (P^3) line of the Clinton P. Anderson Los Alamos Meson Physics Facility, LAMPF. The heart of LAMPF is an 800 Mev, 1 mA (average) proton linear accelerator. The resultant beam is transported to several graphite or alumina targets located just upstream of the various experimental areas, where the proton bombardment results in copious production of pions of all three charges. Pions of desired charge are extracted from this target area at an angle of 20° relative to the incoming proton beam and magnetically transported down the P^3 line towards the target area. The beam line dipole magnets and slits act together to select particles of the desired momentum. The proper settings for the slits and magnets were calculated by an on-site computer program.

The beam used in the present measurement, which had a kinetic energy of 165 Mev, could be delivered to the target with a flux of 2×10^7 pions/second, the full width momentum spread being 1%. Due to pion decays in the beam line, the incoming flux was contaminated with an admixture of $\approx$ 7% μ^- as well as $\approx$ 30% electrons (Br81). This beam was transported through a vacuum pipe to immediately upstream of the target, at which point it exited from the beam line through a Kapton window, crossed a small gap of atmosphere, and entered the target. With the aid of the beam line quadrupoles and a beam profile monitor, the beam spot could be tailored to a circular spot of $\approx$ 2 cm diameter. A logic signal provided by the facility to indicate presence or absence of beam was used to suspend data acquisition during periods of beam shutoff lasting more than a few seconds, which occurred frequently during the experiment and would otherwise have led to an increased background. Further details of

the P^3 line and the LAMPF facility in general can be found in the LAMPF User's Handbook (La80).

C. The Liquid ^{4}He Target System

The cryogenic ^{4}He target system, which is diagrammed in figure 4, had originally been constructed for the purpose of pion nucleus total cross section measurements (Me74). For the purpose of the present measurement, a new cryostat system was mounted above the target cell by the LAMPF cryogenics group.

The target cell itself consists of a 7.57 cm diameter brass cylinder, segmented into two identical chambers, one above the other, as shown in the drawing. Identical windows of 18 mg/cm^2 Kapton ($(C_{22}H_{10}N_2O_5)_N$) were bonded to both the entrance and exit ports of each of the chambers. In operation, only the top chamber was filled with Helium, and the lower chamber served as a dummy for the purpose of background subtraction. The target system was mounted on an electrical hoist, enabling one to lower the desired cell into place.

As shown in the figure, the target cell was soldered to a stainless steel cylindrical tube which connected it to the ^{4}He reservoir above. This tube was in turn surrounded by a liquid nitrogen cooled anti-radiation shield. The entire assembly was enclosed in an external vacuum chamber, which was fitted with additional Kapton windows of 10.8 mg/cm^2 thickness opposite the target positions.

Resistance thermometers mounted at four different heights within the system served as liquid Helium level indicators. After an initial cool-down period, the Helium required replenishment every 8 hours, the Nitrogen every 24.

The target thickness adopted was 0.91 ± .04 g/cm^2. Further details of the target cell's construction are described by Meyer (Me74).

D. The Dipole Magnet

The circular dipole magnet was positioned immediately downstream of the target assembly, and deflected the unreacted π^- beam away from the forward wire chambers of the spectrometer, to prevent their flooding. The magnet consisted of two 30.5 cm diameter circular pole pieces, separated by an air gap of 5.1 cm, and mounted in an H type yoke. Fields of up to 8.5 kG were supplied by the magnet during the spectrometer acceptance scans. To reduce multiple scattering in the atmosphere, a mylar bag filled with gaseous helium was placed in the dipole gap.

E. The Magnetic Spectrometer

Optically, the spectrometer consists of a quadrupole doublet followed by a dipole magnet, which bends the particles upwards by 30°, as shown in figure 3. The quadrupole magnets act as lenses in the x and y planes, thereby focusing divergent particles through the system, and endowing it with a large angular acceptance (nominally 25 msr). The four multiwire proportional chambers of the spectrometer, two of them (W1 and W2) mounted immediately up and downstream of the doublet and two (W3 and W4) downstream of the bending magnet, served to identify the position of the analyzed particle in the chamber planes during its flight through the system. Readout of the chambers was triggered by properly delayed coincidence signals from the three plastic scintillators (S1,S2, and S3), indicating the passage of a particle through the entire spectrometer.

Positional readout of the wire chambers was implemented in two different fashions; the first two chambers used the LeCroy PCOS system, which provides a separate discriminator for each wire and generates a digital output corresponding to the number of the wire(s) that had fired, which can then be processed directly by computer. The two downstream chambers used instead a delay line technique in which all of the wires in a chamber segment are connected to a single delay line, the two ends of which are connected through discriminators to time-to-digital converters (TDCs). By measuring the difference between arrival times at each end, the position along the delay line at which the event has occurred can be determined, with resolution down to the wire spacing. Because of dispersive effects in the delay line which would have degraded positional resolution in a long chamber, the rear detectors were segmented, each segment having its own delay line and readout system.

The rear scintillators, S2 and S3, were each composed of five individual strips of scintillator, 50 cm long, abutted one up against the side of the other to completely cover the focal plane. Due to the large dimensions of this plane the arrival time of an optical pulse at the photomultiplier depends on the position of the trajectory's intersection with the scintillator. In order to eliminate this dependence, S2 and S3 were mounted with their phototubes on the opposite sides of the spectrometer, and their signals sent through a meantimer, which generated an output pulse delayed by a fixed amount relative to the time intermediate between the trigger times of S2 and S3. In effect, this setup calculated the average time of the triggering of S2 and S3, cancelling out the dependence on position.

For the purpose of reducing multiple scattering, a vacuum pipe with thin Kapton windows was placed in the quadrupole gaps, and a Helium bag was positioned between the bending magnet and the rear wire chambers.

F. The Cerenkov Detector

The Cerenkov counter for positron rejection was placed in the rear focal plane of the spectrometer, immediately downstream of scintillator S3, as shown in figure 3.

A particle traveling through a transparent medium at a velocity larger than the local speed of light will emit Cerenkov radiation by a process analogous to the generation of shock waves by projectiles moving through gasses at supersonic speeds. The .511 Mev rest mass of the positron implies that any of these particles possessing sufficient momentum for transmission through the spectrometer (≈200Mev), have $\beta \geq .99999$, while a pion of similar momentum has $\beta \leq .75$. Therefore, in order to discriminate between positrons and pions on the basis of the Cerenkov effect, a radiating medium with an index of refraction n such that

$$.75 \leq n^{-1} \leq .99999$$

must be used. In fact, it was deemed desirable to construct a counter which would not trigger on pions of momenta less than 420 Mev, ($\beta \leq .95$), making the device useful for higher energy measurements as well. This requirement necessitated a radiator with $n \leq 1.05$. Although Cerenkov detectors can be built using gasses such a Freon or propane (usually under pressure), it is far more convenient to use a solid if possible.

One of the few solids with indices of refraction suitable for use in this velocity range is Silica Aerogel ($(SiO_2+2(H_2O)_n)$, an extremely fragile and

hygroscopic material which is available with $1.01 \leq n \leq 1.10$. Forty blocks of $n=1.050$ ($\pm$ .001) Aerogel were procured*, each block measuring 19.2 cm square by 3.0 cm thick. Roughly 15% of the blocks supplied had clearly visible internal bubbles and cracks, but these had little effect on the operation of the counter.

Figure 5 shows the design of the counter, which was constructed of .125 inch aluminum sheet secured to a frame of .25 inch square aluminum stock with brass screws. The detector, basically a box 41 inches long by 20 inches wide by 13 inches high, is divided into two sections, the upper (upstream) 5 inches being the cell containing the Aerogel radiating material, the lower 8 acting as a diffusing box to reflect the Cerenkov photons into the 10 photomultiplier tubes mounted along the sides. The Aerogel blocks were cut with a dry carborundum saw and fitted into the upper cell, a network of fine cords serving to restrain the material from falling into the diffusing box. It should be noted that the cutting process generated large amounts of hazardous dust, and had to be carried out with the protection of a suitable filtering mask. The top and bottom cover plates were cut from .062 inch aluminum.

The diffusing box section of the counter was segmented by aluminum partitions into 5 smaller parts, one for each pair of phototubes. The entire surface of the diffusing box was sprayed with 8 coats of Eastman 6080 White Reflectance Coating, a substance possessing very high reflectivity in the near ultraviolet region, where the Cerenkov emission is strongest. The phototubes, RCA 4522s, were mounted along the sides of the box. These 14 stage tubes, 5 inches in diameter, were selected for

*Dr. Sten Henning, Physics Department
Sölvegatan 14, S-223 62 LUND, Sweden

their high quantum efficiency (≈29% at 360 nm), high gain (typically 2.5 $\times 10^7$), and large active faceplate area. The phototubes were enclosed in aluminum "cans" welded to the sides of the counter, with removable retaining rings fitted with O-ring seals serving to constrain the phototubes and shield out stray light. Tube replacement was much more convenient with this system than conventional methods employing silicone adhesive as the light sealant. The cans were surrounded with mu-metal cylinders to shield the photomultipliers against stray magnetic fields from the spectrometer.

A prototype counter a single segment wide was constructed, and used to evaluate the efficiency of the larger detector at detecting cosmic ray muons. A telescope consisting of, topmost, a 5 inch square scintillator paddle, then the small Cerenkov counter, next, the large counter, and finally, another paddle, was assembled. The two paddles, which served to define the direction of the cosmic ray, and the small counter, which selected particles moving above the Cerenkov threshold velocity, were run in coincidence, each pulse being tallied on a scaler, this number being compared with the number of coincidences between all four detectors, the efficiency of the large counter being simply the ratio of the latter number to the former. With 3 kV on the tubes, and the discriminator outputs of the two tubes being logically ORed together, efficiencies of 97% to 99% were measured for each segment.

Table 2 shows the efficiency of the Cerenkov detector as mounted on the back of the spectrometer at Los Alamos, tabulated as a function of the relative momentum of the triggering particle. This was determined by bombarding a CH_2 target at the front focus of the spectrometer with a 165 Mev negative beam, and observing the momentum spectrum of the

resulting positrons (produced primarily by beam electrons) both in coincidence with and unwindowed on the Cerenkov pulses. Because all of the positrons are fast enough to generate Cerenkov light, the efficiency of the counter for a given relative momentum (which corresponds to a definite position along the length of the counter), is given by the ratio of the number of counts measured in the coincidence mode to the unwindowed figure. These efficiency figures, corresponding by Poisson statistics to 4 or 5 photoelectrons produced for every positron, are slightly smaller than the 10 or so photoelectrons that one calculates assuming 10% photon collection efficiency and typical Cerenkov light yields of 50 photons per centimeter of radiating material. This discrepancy is due, at least in part, to the absorption of photons in the Aerogel, as the absorptivity of the material rises strongly with decreasing wavelength.

G. The Beam Monitor

The directions of those muons arising from the decay of pions in the incident 165 Mev beam are kinematically confined to a cone of 9.3° (half-angle) about the forward direction. By monitoring the flux of these decay muons it was possible to normalize the runs relative to one another.

Identical pairs of scintillator paddles were mounted to the right and left of the beam line just upstream of the Helium target, as shown in figure 6. "Halo" muons transmitted through the windows as shown triggered either the right or left pair of detectors. Each of these pairs was run in coincidence mode in order to define the direction of the triggering particle as coming from the beam, and thereby cut down on background from stray radiation in the target area. The counts from the left and right detector arrays were summed and recorded with scalers. The left-right

symmetry of the arrangement was designed to reduce the dependence of the count rate on the angle of the beam relative to the beam line axis.

Under typical beam conditions, the monitor triggered at a frequency of 1 kHz.

H. Electronics

Figure 7 is a simplified functional schematic of the electronics for the measurement. Eliminated for the sake of clarity are numerous delay line boxes, fan-in and fan-outs, scalers, discriminators and preamplifiers.

The trigger and wire chamber circuitry was located in the P^3 cave, mounted on the spectrometer itself, while the rest of the electronics was outside the radiation shield in the data acquisition trailer. Of the latter, the various ADCs, TDCs, and scalers were mounted in CAMAC "crates" for direct readout by the PDP-11/45. Occurrence of an event generating a coincidence between S1, S2, and S3 triggered the writing of the event parameters (wire chamber outputs, time of flight, and Cerenkov output) onto magnetic tape.

During the initial phases of the experiment the electronics were configured so as to process every signal creating a scintillator coincidence in the spectrometer, regardless of its Cerenkov status, and leaving elimination of positrons to software analysis. The count rate, however, proved excessive with this arrangement, resulting in very significant dead times as well as unacceptably high magnetic tape consumption rates. The electronics were therefore reconfigured to reject 9 out of every 10 events that triggered the Cerenkov detector, leaving the tenth event to the software. An additional acceptance criterion added was the requirement that the horizontal plane of wire chamber number 3 fire (that chamber

plane being unsegmented), in order to avoid processing events that would have to be rejected during data analysis anyway. These modifications are shown in figure 7b. With this setup the dead time was brought down to under 3%.

VI. Experimental Procedure

A. Acceptance Scans

The angular acceptance of the magnetic spectrometer varies as a function of the relative $\frac{\Delta p}{p}$ of the particles being detected, and the measured momentum spectrum must therefore be corrected for this deviation. This variation was measured by observation of the number of recoil protons from $\pi^- p$ elastic scattering at 180° as a function of its momentum channel.

The Helium target was replaced by a .250 g/cm^2 slab of polyethylene ($(CH_2)_n$). The energy, momentum bite, and beam profile characteristics of the π^- were identical to those used for the double charge exchange runs. The spectrometer was rotated to 11.6° relative to the incident beam, and the circular dipole magnet current scaled upwards to the value appropriate to the 180° recoiling protons being bent into the spectrometer. With this magnet setting remaining fixed, the spectrometer bending and focusing quadrupoles magnet currents were stepped upwards and downwards, with a short (≈10,000 counts in the elastic peak for 1% statistics) measurement being taken at each magnet setting. For each point, the magnet settings, number of counts in the elastic peak, beam flux decay muon count, dead time and spectrometer efficiency parameters were recorded. Reproducibility was verified by going back down to the low magnetic field data points after the higher field ones, and agreement was obtained within statistical error bars.

A typical proton momentum spectrum from an acceptance run is shown in figure 8. The broad background below the strong elastic peak is due to scattering from Fermi broadened protons in ^{12}C nuclei in the

polyethylene, and was subtracted by approximating the behavior under the peak by a straight line.

The relative acceptance of the spectrometer is defined by the relation

$$A = \frac{c}{\frac{d\sigma}{d\Omega} \cdot \pi \rightarrow \mu_{eff} \cdot t}$$

where

c = proton counts in elastic peak

$\frac{d\sigma}{d\Omega}$ = 180° lab frame differential cross section for $\pi^- p$ elastic scattering (measured per unit *proton* solid angle)

t = number of hydrogen nuclei per unit target area

$\pi \rightarrow \mu_{eff}$ = "effective" number of decay muons detected by beam flux monitor (as defined in section VII. G)

The relative acceptance so defined is actually the angular acceptance of the spectrometer divided by the efficiency of the beam flux monitor. By using this relative acceptance in the extraction of the double charge exchange cross section, one eliminates the requirement of an *absolute* measurement of either the beam flux or spectrometer acceptance, as only the product of the two appears in the final calculation.

The measured relative acceptance is shown in figure 9 and table 1.

B. Dipole Magnet Calibration

For a particle of unit charge, the product of momentum and angular deflection is proportional to the magnetic field of the bending magnet. In order to determine this constant of proportionality for the circular dipole, knowledge of which is necessary in order to determine the 0° point needed for the DCX measurement as well as for the energy calibration, a small, uncalibrated ion chamber was mounted at 15° relative to the beam axis, a 165 Mev (270.7 Mev/c) beam run through the dipole, and the magnet current varied until the flux passing through the chamber peaked, which occurred at 220 Amperes. The curve of magnet central field versus current had been previously measured with an NMR probe, showing that this current corresponded to a field of 6.35 kG, and fixing the above mentioned constant at $639.5 \pm 1.0 \frac{°Mev/c}{kG}$.

C. Energy Calibration

In order to accurately fix the zero binding energy point of the π^+ momentum spectrum, the $^{12}C(\pi^-,\pi^+)^{12}Be$ reaction was used as a reference marker. A natural Carbon target of 1.306 g/cm^2 thickness replaced the liquid Helium, and the spectrometer was moved to 22° relative to the beam line. The beam channel and spectrometer magnets were left at the same settings used for the Helium DCX runs, but the circular dipole current was reduced so as to deflect the π^+ by 14°, putting the spectrometer at 8° relative to the 0° π^+ because positron background proved prohibitive at smaller angles.

The π^+ momentum spectrum shown in figure 10, with a prominent peak due to transitions to the ^{12}Be ground and low lying excited states, was accumulated after 1.5 hours of running time. Using the ^{12}Be atomic

mass excess of 25.078 Mev (Al78), one arrives at a Q value of -26.1 Mev for the ground state-ground state reaction. Correcting for pion energy loss in the Carbon target (1.6 Mev cm^2/g at 165 Mev), a value of 238.3 Mev/c for those pions due to the ground state transition was arrived at. Seth *et al* (Se78) finds first and second excited states in ^{12}Be at 2.09 and 2.71 Mev, respectively, which are excited in (π^-,π^+) almost as strongly as the ground state, and these were accounted for in the energy calibration.

D. Helium Runs

With an Ar–CO_2 wire chamber serving as a beam profile monitor, the beam was focused to circular spot 2 cm in diameter. DCX runs were attempted with the profile monitor in place, but the additional background proved excessive, and it was removed. It was reinserted between data acquisition runs as a check on the stability of the beam profile.

Data acquisition was interrupted every 2 to 3 hours, and the on-line spectra as well as system scalers dumped to magnetic tape. The spectrometer magnet settings as well as those of the channel were inspected every hour as a check on their stability, and recorded every few runs. Occasionally the current supplies powering the channel magnets or the wire chambers would shut themselves off, causing those runs to be lost. Later in the experiment, alarms were installed to alert the experimenters of such eventualities, and minimize wasted time. The target cryogenic liquids and wire chamber gasses were also replenished during these data acquisition suspensions.

Although the method of data reduction makes an absolute determination of the beam flux unnecessary, a rough check is made possible by assuming the circular dipole + spectrometer acceptance to equal the

ALAS nominal value of 25 msr (probably an overestimate, as the presence of the circular dipole will certainly tend to reduce it), and coupling the well known value for $\pi^- p$ elastic scattering with the acceptance run results. The value arrived at was $\approx 2\times10^6$/second, a result confirmed by the ion chamber current reading. This figure is smaller than the nominal P^3 π^- flux by roughly an order of magnitude, which is not surprising in view of the fact that the LAMPF linac was being run at an average proton flux of only .5 mA (as opposed to a nominal value of 1 mA) during the runs, as well as the circumstance that a thinner pion production target than usual was in use.

E. Background Subtraction Runs

After the first 24 hours of Helium data acquisition, the target system was raised to bring the blank cell into position for the background subtraction runs. The profile monitor was left out of the beam for these measurements. Aside from the target used, the background runs were in all respects identical to those for Helium. 18 hours of background were accumulated, and then the Helium cell was relowered into position for another 52 hours of bombardment. A final 37 hours of background running completed the measurement.

VII. Data Analysis

A. Software

The data analysis was carried out off-line on the Kellogg VAX-11/750 computer. All of the analysis routines were written in the FORTRAN language.

Each hardware accepted event triggered the creation of a 32 word buffer containing the outputs of the wire chamber TDCs, the PCOS chamber event descriptors, the time of flight value, the scintillator ADC outputs, and a word indicating whether or not the Cerenkov detector had fired. These were buffered on the PDP-11, and written to magnetic tape in groups of 32 events each. Every event buffer written to tape was processed by first converting the wire chamber PCOS and TDC parameters to physical positions in the chamber planes, two (one for x and one for y) for each of the four chambers, these positions being defined relative to the spectrometer fiducial central trajectory. The PCOS results were then inspected to determine that all four PCOS chamber planes had fired, and the sum of the delay line data for each chamber segment was checked for consistency with the known total delay time for the line in question, with inconsistent events, corresponding to multiple hits in a chamber, being discarded. It was further determined whether exactly one delay line chamber segment per plane had fired, and those for which such was not the case were rejected.

Next, using the algorithm of Kulaga and Geesaman (Ku81) the parameters of the event at the target were evaluated. Five parameters suffice to completely characterize an event; the x and y positions of the π^+ at the target, x_0 and y_0, the angles made by the π^+ at the target relative to

the central trajectory projected on the local x and y axes, x_0' and y_0', and the particle's relative momentum deviation, $\frac{\Delta p}{p}$. These quantities are assembled into a 5 × 1 column matrix called α. Similarly, the eight x and y positions of the π^+ at the 4 wire chambers make up the elements of the 8 × 1 column matrix **T**. If the randomness introduced by the statistical nature of multiple scattering in the spectrometer is ignored, the elements of α, representing the production coordinates of the π^+, completely determine the particle's trajectory through the spectrometer, and hence the intersections of the path with the wire chamber planes, the positions of which constitute the elements of **T**. The functional relationship between α and **T** can be expanded in a power series about α. The coefficients of this power series were evaluated at Argonne National Laboratory using the computer code RAYTRACE (Ko68). With these coefficients in hand, a multidimensional, weighted version of the Newton-Raphson method (So64,Br70) was used to recursively determine the value of α best fitting the measured elements of **T**, and a χ^2 "goodness of fit" parameter was evaluated for each event so processed.

The analysis software provided for the accumulation of each of the components of α, as well as any of the elements of the event buffers, into spectra of up to 2048 channels. It was also possible to window the events being accumulated into each of the spectra on any of the other parameters of the event, such as time of flight, Cerenkov pulse, or χ^2 value. This capability was used to eliminate those background events due to contaminant particles.

B. Background Reduction

The $\frac{\Delta p}{p}$ spectrum for each of the runs was initially binned into 256 channels, with each channel representing a 0.2% momentum bite. These raw spectra were then further compressed by a factor of five, resulting in a $\frac{\Delta p}{p}$ of 1.0% per channel, in order to match the momentum spread of the incoming π^- beam, which represented the limiting factor of the energy resolution of the experiment.

A major background problem for the cross section measurement was posed by the production in the target of positrons of proper momentum for transmission through the spectrometer, which could thereby masquerade as π^+ particles. These positrons can be produced by two primary mechanisms: Firstly, a beam π^- can undergo *single* charge exchange to a π^0,

$$\pi^- + {}^4\mathrm{He} \rightarrow \pi^0 + {}^4\mathrm{H}$$

the resulting π^0 immediately undergoing electromagnetic decay to 2 gamma rays,

$$\pi^0 \rightarrow 2\gamma$$

and each of the gammas may pair produce in the electrical field of the target nuclei,

$$\gamma \rightarrow e^+ + e^-.$$

Another mechanism for production of positrons is provided by the pair production of electrons and positrons by contaminant electrons in the beam on target nuclei

$$e^- + {}^4He \rightarrow {}^4He + e^+ + 2e^-.$$

The anticipated count rate due entirely to the π^0 mechanism was of the order of 1 Hz for a flux of $10^7\pi^-$/second. In practice, the positron count rate within the spectrometer acceptance was found to be typically on the order of 5 Hz, even though the beam flux was only of the order of 10^6/second. This can be attributed to higher electron contamination in the π^- beam than expected. The pion count rate within the spectrometer momentum acceptance range was less than this by a factor of $\approx$ 400.

In order to weed out the positrons, the events were judged by two criteria: their time of flight through the spectrometer, and presence of a coincident Cerenkov pulse.

A typical time of flight spectrum is shown in figure 11. One can see that while the positrons are clearly separated from the pions on the basis of time of flight alone, the relative count rates are such that the tail of the electron peak would still overwhelm the pion signal. To further reduce positron contamination, the event acceptance requirement of anticoincidence with the Cerenkov detector was imposed. Coupled with the $\approx$ hundred-fold reduction in positrons made by the time of flight window, the overall positron count rate was reduced to $\leq$5% of that of the pions.

The other major particle contaminants were positive muons created during the in-spectrometer decay

$$\pi^+ \rightarrow \mu^+ + \nu_\mu$$

of the π^+ produced by DCX in the target. The ν_μ is of course unobserved, and hence imparts a randomly directed momentum impulse to the μ^+,

changing that particle's trajectory sharply, and thereby generating spurious counts in random parts of the momentum spectrum. These muon events were removed by placing an acceptance window on the χ^2 value of the event. Pions decaying in flight through the spectrometer will in general have sharp discontinuities in their directions at the decay point and therefore give poor fits to the measured **T** for any value of α, (remembering that **T** is 8 elements being fitted to only 5 parameters), and can therefore be distinguished from the surviving pions on the basis of their large χ^2 values.

Figure 12 is a typical run's χ^2 spectrum, showing the location of the window positions selected for acceptance criteria. If this curve is fitted to a χ^2 curve for three degrees of freedom, one sees that the window limit shown at channel 76 will result in the rejection of less than 1% of the undecayed pions, while the muons, being distributed evenly across the χ^2 spectrum, will be preferentially rejected. According to the Monte Carlo simulation of Colton (Co80), less than one muon in five will fall within the acceptance window.

The relativistic expression for the number of pions passing from the front wire chamber to the focal plane scintillators without undergoing decay is given by

$$f=1-\exp\left(-\frac{m_\pi l}{pc\tau}\right)$$

where

f = fraction of pions surviving

m_π = pion mass (139.6 Mev)

l = path length through the spectrometer (469.8 cm)

p = pion momentum

τ = pion lifetime at rest (2.603×10^{-8}seconds)

c = speed of light

For 240 Mev/c pions, 29.5% will undergo decay in the spectrometer. Folding in the abovementioned muon rejection factor of five, it is seen that less than 6% of the observed counts are due to muons, and because of the random impulse imparted to the decay muon, those that are not rejected are unlikely to contribute any structure to the spectrum, forming instead a relatively flat background.

C. Spectrometer Efficiency

The spectrometer efficiency was reevaluated for each run using the following procedure (Ku81). For each hardware accepted event, a bit pattern indicating which of the eight wire chamber planes fired was recorded. The efficiency of, for example, chamber 1x, was then determined by the quotient

$$E_{1x} = \frac{1x \cdot 2x \cdot 3x \cdot 4x \cdot 1y \cdot 2y \cdot 3y \cdot 4y}{2x \cdot 3x \cdot 4x \cdot 1y \cdot 2y \cdot 3y \cdot 4y}$$

where · denotes the logical AND operation, $1x$ represents the firing of chamber plane $1x$, and so forth for the other chambers. Therefore, the denominator of the expression indicates the number of times during the run that the other 7 chamber planes fired, irrespective of whether chamber $1x$ fired as well, while the numerator is the number of those events for which chamber $1x$ fired as well. The overall spectrometer efficiency can then be evaluated by simply taking the product of the efficiencies of the individual chambers.

Typical chamber efficiencies are displayed in table 3.

D. Flux evaluation

The π^- decay muon counts used for normalization purposes must be corrected for the varying computer dead time and spectrometer efficiency before the counts for each run could be summed. Therefore, an effective decay muon count was defined as

$$\pi\rightarrow\mu_{eff}=\pi\rightarrow\mu\cdot effy\cdot live \qquad (7.1)$$

with

$$live=\frac{s1\cdot s2\cdot s3\cdot free}{s1\cdot s2\cdot s3}$$

where

$\pi\rightarrow\mu_{eff}$ = corrected decay muon count

$\pi\rightarrow\mu$ = raw decay muon count

$s1\cdot s2\cdot s3$= total number of events coincident in all three scintillators

effy = overall wire chamber efficiency of spectrometer

free = register indicating computer readiness to accept new event

live = fractional live time of computer

The $\pi\rightarrow\mu_{eff}$ values for each run were then summed to give an overall figure for the Helium runs.

E. Background Subtraction

Exactly as for the case of the ^{4}He runs, the 256 channel spectra of the background runs were summed and compressed by a factor of five. In order to smooth out the statistical fluctuations in the background spectrum, a third order polynomial was fitted to the spectrum, as shown in

figure 13. This curve, weighted by the ratio of the effective decay muon monitor counts of the ^{4}He to those of the background runs, was then subtracted from the summed Helium spectrum. Direct bin by bin subtraction of the background spectrum from the Helium spectrum was also tried, yielding results virtually indistinguishable from the indirect method.

F. Cross Section Extraction

The final expression for the differential cross section of the reaction is given by

$$\frac{d\sigma}{dpd\Omega} = \frac{y}{\pi \rightarrow \mu_{eff} \cdot t \Delta \cdot A \cdot d}$$

where

$\frac{d\sigma}{dpd\Omega}$ = cross section per unit solid angle per unit momentum (in the lab frame)

y = net counts in spectrum bin

$\pi \rightarrow \mu_{eff}$ = effective decay muon counts

t = target thickness

Δ = momentum bite per bin

A = acceptance of spectrometer for given bin

d = fraction of pions not undergoing decay in spectrometer = 1-f

Poisson statistics give the error bars for each point to equal $\frac{d\sigma}{dpd\Omega}$ divided by the square root of the number of counts in the given bin.

The resultant spectrum is shown in figure 14, and in table 4.

G. Error Analysis

Equation (7.1) gives the corrected value of $\pi \to \mu$. Using standard expressions for the propagation of errors, we have

$$\frac{\sigma^2_{\pi\to\mu_{eff_i}}}{\pi\to\mu_{eff_i}{}^2} = \frac{\sigma^2_{\pi\to\mu_i}}{\pi\to\mu_i{}^2} + \frac{\sigma^2_{live}}{live^2} + \frac{\sigma^2_{effy}}{effy^2}$$

where the subscript i denotes the run number. The various contributions to this expression are given by:

$$\frac{\sigma^2_{\pi\to\mu_i}}{\pi\to\mu_i{}^2} = \frac{1}{\pi\to\mu_i}$$

by Poisson statistics,

$$\frac{\sigma^2_{live}}{live^2} = \frac{1-live}{live\cdot s1\cdot s2\cdot s3}$$

using Binomial statistics,

$$\frac{\sigma^2_{effy}}{effy^2} = \sum_{j=1}^{j=8} \frac{\sigma^2_{E_j}}{E_j{}^2} \quad ,$$

where the subscript j denotes the wire chamber plane, and

$$\frac{\sigma_{E_j^2}}{E_j{}^2} = \frac{1-E_j}{E_j\cdot N}$$

again by Binomial statistics, where

$$N = 1x\cdot 2x\cdot 3x\cdot 4x\cdot 1y\cdot 2y\cdot 3y\cdot 4y$$

In practice, the first term in this equation was negligible compared with the other two, which were of comparable magnitude to each other.

The total standard deviation is given by

$$\sigma^2_{\pi\to\mu_{eff}} = \sum_i \sigma^2_{\pi\to\mu_{eff}i} \quad .$$

The $\pi\to\mu$ values and estimated errors for the ^{4}He and background runs are to be found in table 5.

Systematic errors are due mainly to uncertainty in the basic $\pi^- p$ cross section at 0° , (± 3%), which entered into the acceptance determination, and the thickness of the Helium target (± 4%). Adding these two relative errors in quadrature gives an overall uncertainty of 5%, completely dominating that due to the beam monitor statistics, which contributed less than 1%.

VIII. Results and Conclusions

A. Bound Tetraneutron Production

The final DCX spectrum, shown in figure 14, drops to a cross section of zero at exactly the momentum corresponding to four unbound neutrons in the final state, as determined by the $^{12}C(\pi^-,\pi^+)^{12}Be$ calibration reaction. There are, nevertheless, a few π^+ counts to be found at energies higher than this value, and indeed several to be found above the 3.1 Mev binding limit of the tetraneutron. Some of these are due to positrons having slipped through the time-of-flight and Cerenkov rejection windows. As discussed previously, positrons are produced either in pair production showers or by the two step process involving the π^0, and their numbers will therefore grow nonlinearly with target thickness, making their elimination through simple subtraction impossible. A contribution to these points is also due to π^+ decay muons, as rejection was not 100% efficient. A straight line was fitted to the high momentum ($\geq$ 240 Mev/c) points, and this background curve was subtracted from the lower energy points. Adding up the contributions of data points between 0 and 3.1 Mev binding, one arrives at a figure of 7±15 nb/sr for tetraneutron production by this reaction.

B. Issues Relating to the DCX Reaction Mechanism

Figure 15 shows the 140 Mev, 20° (lab) data of Kaufman *et al* (Ka67,68). Although direct comparison of that measurement with the present work is difficult because of the different somewhat different kinematic regions sampled, it is reasonable to appeal to the results of, for example, Falomkin *et al* (Fa74,76) which show a rather mild

dependence of cross section on bombarding energy in the region of 150 Mev (in contrast to the elementary pion-nucleon interaction which is, of course, strongly energy dependent), as well as the results of Stetz *et al* (St81) who find mild, smooth angular distributions to conclude that these two measurements should agree, at least within an order of magnitude. The cross sections measured in the present experiment are between 100 and 200 times as large as those found in the earlier experiment at comparable excitation energies. It seems impossible to reconcile the two measurements, and in view of similar discrepancies between the Kaufman *et al* data and those of other related experiments it appears that the earlier experiment was in error, at least as far as normalization is concerned.

In view of the excellent agreement between the data of Kaufman *et al* and the theoretical predictions of Gibbs *et al*, it seems most unlikely that these calculations can reproduce the present experimental results. If no error in the calculations can be found, perhaps another mechanism should be appealed to.

C. Shape of the Continuum

If the underlying transition matrix element for the process is independent of the particular distribution of momentum amongst the five final state particles, the energy spectrum can easily be evaluated as a phase space integral, up to an overall multiplicative factor. To determine whether dynamical effects are important in determining the spectrum shape, such a phase space curve, corresponding to four free final state neutrons, and with no allowance for Pauli principle effects, was least-square fitted to the data, as shown in figure 16.

Even if the underlying DCX matrix element is independent of the momentum distribution of the final state particles, the spectrum shape can still be distorted from the phase space result because of the effects of the attractive nucleon-nucleon force acting between the neutrons, which will tend to enhance final states in which the interacting nucleons have small relative momenta. In the kinematic region corresponding to the four neutrons having little kinetic energy in their center of mass frame, which is the area investigated in this measurement, the neutron-neutron force can be well represented by scattering length theory. At low energies, the neutrons will interact primarily in relative s states, which by the Pauli principle restricts their relative spin states to singlets. Using the average of the neutron-neutron scattering length figures quoted by Preston and Bhaduri (Pr75), curves were calculated for the case in which only one of the two pairs of neutrons interact, as well as the case in which there are two such interacting pairs, and the results were least-square fitted to the data and displayed with the results of the pure phase space calculation. The χ^2_ν values for the three calculations are displayed in table 6.

Previous investigators of the $^4He(\pi^-,\pi^+)4n$ reaction have also included the effects of final state interactions in their analyses. Gilly *et al* (Gi65), in explaining the deviation of their curve of cross section versus incident π^- energy from a 4 neutron phase space, invoked the final state interaction between a single pair of final state neutrons to fit the data. Becker and Schmit (Be70) in their analysis of the Gilly *et al* experiment, found that the influence of the Δ resonance in the pion-nucleon interaction was much more important in determining the shape of this curve than the final state interaction, although including such an interaction

gave improved agreement with the data.

Kaufman *et al* (Ka67,68), who, as in the present experiment, have looked at the spectrum of the outgoing π^+ for fixed π^- energy, also fitted phase space curves and curves with final state interactions to their data. They found best agreement with a curve corresponding to a single interacting neutron pair. As stated before, the usefulness of the results of that experiment are questionable, although if the discrepancy with other measurements is due only to an overall normalization error, their results may still be relevant to the question of the importance of final state interactions.

The present experiment shows best agreement with the curve calculated for two interacting pairs, although even here the confidence level is below 1%, indicating that other dynamical effects are at work. In any event, a consistent treatment of final state interactions in a system with four particles would have to include the interactions between all of the particles and not only one or two pairs, as well as Pauli effects, which all calculations show to be more important in $^4He(\pi^-,\pi^+)4n$ than the pairwise final state interactions. Unfortunately, the theoretical tools for investigating final state effects in systems with more than three particles are not as yet highly developed. A problem in analyzing data from reactions which leave multiparticle final states is that of sorting out the effects of genuine multiparticle resonances from spectral structure due entirely to simple pairwise interactions, which has led to confusion with respect to interpretation of data purporting to show trineutron resonances, for example.

If a four neutron resonance does indeed exist, one can place an upper limit on its decay width to a pair of dineutron resonances using R

matrix theory. Teichman and Wigner (Te52) have shown that

$$\gamma_a^2 \leq \frac{3h^2}{8\pi^2 M a_c}$$

where

a_c = channel radius

γ_a^2 = reduced decay width appropriate to the chosen channel radius

h = Planck's constant

M = reduced mass of the two dineutron system

The decay width of the resonance is then given by

$$\Gamma = 2kv_l\gamma_a^2$$

where

Γ = decay width of the 4 neutron resonance

k = relative motion wavenumber of the two dineutrons

v_l = penetration function (in the l'th partial wave) for the two dineutrons

If one adopts a channel radius of 3.5 fm for the decay, and allows the dineutrons to interact in an s-wave, a resonance 10 Mev above binding has a width of less than 25 Mev. Figure 14 shows no structure outside of the statistical error bars, which are typically of the order of 5 nb/(sr Mev/c), leading to an estimated upper limit (at the one-sigma level of confidence) of 125 nb for a four neutron resonance 10 Mev or less from binding.

D. Directions for Further Investigation

Understanding of the nature of the $^4He(\pi^-,\pi^+)4n$ reaction would certainly be deepened if angular distribution measurements could be carried out. Comparison of these distributions with the highly diffractive shapes seen in DCX on heavier nuclei would certainly yield valuable information about the changing role of reaction mechanism as the mass of the target is varied.

If the $^4He(\pi^-,\pi^+)4n$ reaction indeed does proceed by way of two sequential steps of SCX, it passes through an intermediate stage consisting of π^0 + p + 3n. At low momentum transfer, the virtual π^0 is very close to its energy shell, and it might prove instructive to compare the present results to a measurement of $^4He(\pi^-,\pi^0)p3n$.

Double charge exchange reactions at energies in the hundreds of Mev range, first suggested as a probe of interesting nuclear properties almost twenty years ago, have resolutely resisted theoretical attempts at detailed predictions, in no small part because of the dearth of experimental results with which to compare these calculations. It is to be hoped that continuing experimentation in the field, together with improved calculations, will lead to a successful microscopic understanding of the process, and thereby enable its use as a tool in furthering our understanding of nucleon correlations and mesonic degrees of freedom in nuclei.

REFERENCES

Al78 D. E. Alburger, S. Mordechai, H. T. Fortune and R. Middleton, Physical Review **C18**, 2727(1978)

Am64 Amaldi *et al*, Inst. Sup. de Sanita (Rome), Report ISS 64/65

Ar63 P. E. Argan and A. Piazzoli, Physics Letters **4**, 350(1963)

Ba68a A. M. Badalyan, E. S. Gal'pern, V. N. Lyakhovitskii, V. V. Pustovalov, Yu. A. Siminov and E. L. Surkov, Soviet Journal of Nuclear Physics **6**, 345(1968)

Ba68b Yu. A. Batusov, V. I. Kochkin, and V. M. Mal'tsev, Soviet Journal of Nuclear Physics **6**, 116(1968)

Be70 F. Becker and C. Schmit, Nuclear Physics **B18**, 607(1970)

Be71 F. Becker, Yu. A. Batusov, Revista del Nuovo Cimento **1**, 309(1971)

Br64 O. D. Brill, N. I. Venikov, A. A. Kuraschov, A. A. Ogloblin, V. M. Pankratov, and V. P. Rudakov, Physics Letters **12**, 51(1964)

Br70 S. Brandt, *Statistical and Computational Methods in Data Analysis*, North-Holland, Amsterdam(1970)

Br81 W. J. Briscoe, D. H. Fitzgerald, B. M. K. Nefkens, and M. E. Sadler, Los Alamos National Report LA-UR 81-2537

Br82 G. E. Brown, H. Toki, W. Weise, A. Wirzba, to be published

Ca68 N. Carayannopoulos, J. Head, N. Kwak, J. Manweiler, and R. Stump, Physical Review Letters **20**, 1215(1968)

Ce74J. Cerny, R. B. Weisenmiller, N. A. Jelley, K. H. Wilcox and G. J. Wozniak, Physics Letters **53B**, 247(1974)

Ci65S. Cierjacks, G. Markus, W. Michaelis, and W. Pönitz, Physical Review **137**, B345(1965)

Co65R. C. Cohen, A. D. Kanaris, S. Margulies, and J. L. Rosen, Physics Letters **16**, 292(1965)

Co79M. D. Cooper in *Proceedings of the LAMPF Workshop on Pion Single Charge Exchange*, Los Alamos National Laboratory report LA-7892-C

Co80E. Colton, Nuclear Instruments and Methods **178**, 95(1980)

Da64aO. D. Dalkarov and I. S. Shapiro, Physics Letters **26B**, 706(1964)

Da64bR. E. P. Davis, A. Beretvas, N. E. Booth, C. Dolnick, R. J. Esterling, R. E. Hill, M. Raymond, and D. Sherden, Bulletin of the American Physical Society **9**, 627(1964)

Fa74I. V. Falomkin, M. M. Kulyukin, V. I. Lyashenko, G. B. Pontecorvo, Yu. A. Shcherbakov, C. Georgescu, A. Mihul, F. Nichitiu, A. Sararu, and G. Piragino, Nuovo Cimento **22A**, 333(1974)

Fa76I. V. Falomkin, V. I. Lyashenko, G. B. Pontecorvo, Yu. Shcherbakov, M. Albu, T. Angelescu, O. Balea, A. Mihul, F. Nichitiu, A. Seraru, F. Balestra, R. Garfagnini, G. Piragino, C. Guaraldo, and R. Scrimaglio, Lettre al Nuovo Cimento **16**, 525(1976)

Fi73S. Fiarman and W. Meyerhof, Nuclear Physics **A206**, 4(1973)

Ge75 J.-F. Germond and C. Wilkin, Lettre al Nuovo Cimento **13**, 605(1975)

Ge79 J.-F. Germond and C. Wilkin, in *Mesons in Nuclei*, Volume II, M. Rho and D. Wilkinson (editors) North-Holland, Amsterdam (1979)

Gi65 L. Gilly, M. Jean, R. Meunier, M. Spighel, J. P. Stroot, and P. Duteil, Physics Letters **19**, 335(1965)

Gi77 W. R. Gibbs, B. F. Gibson, A. T. Hess, and G. J. Stephenson, Jr., Physical Review **C15**, 1384(1977)

Gr82 S. J. Greene, W. J. Braithwaite, D. B. Holtkamp, W. B. Cottingame, C. F. Moore, G. R. Burleson, G. S. Blanpied, A. J. Viescas, G. H. Daw, C. L. Morris, and H. A. Thiessen, Physical Review **C25**, 927(1982)

Je80 J.-B. Jeanneret, M. Bogdanski, and E. Jeannet, Nuclear Physics **A350**, 345(1980)

Jo80 M. B. Johnson, Physical Review **C22**, 192(1980)

Ka67 L. Kaufman, V. Perez-Mendez, J. Sperinde and S. H. Williams, Physics Letters **25B**, 536(1967)

Ka68 L. Kaufman, V. Perez-Mendez, and J. Sperinde, Physical Review **175**, 1358(1968)

Ko68 S. Kowalski, RAYTRACE (1968), unpublished

Ku81 J. Kulaga and D. Geesaman, Argonne National Laboratory internal report

La80 LAMPF Users Handbook, Los Alamos National Laboratory report MP-DO-1-UHB(Revised) p6A.-11(1980)

Me68 W. Meyerhof and T. A. Tombrello, Nuclear Physics **A109**, 1(1968)

Me74 H. O. Meyer, Nuclear Instruments and Methods **120**, 143(1974)

No71 C. Noak, private communication reported by Be71

Pa65 R. G. Parsons, J. S. Trefil, and S. D. Drell, Physical Review **138**, *B847(1965)*

Pr75 M. A. Preston and R. K. Bhaduri, *Structure of the Nucleus*, Addison-Wesley, New York, p.51(1975)

Sc63 J. P. Schiffer and R. Vandenbosch, Physics Letters **5**, 292(1963)

Sc80 J. P. Schiffer, Nuclear Physics **A335**, 339(1980)

Se78 K. K. Seth, H. Nann, S. Iverson, M. Kaletka, J.Hird, and H. A. Thiessen, Physical Review Letters **41**, 1589(1978)

Se79 K. K. Seth in *Proceedings of the LAMPF Workshop on Pion Single Charge Exchange*, Los Alamos National Laboratory report LA-7892-C

Si66 Yu. A. Siminov, Soviet Journal of Nuclear Physics **3**, 461(1966)

So64 F. T. Solmitz, Annual Review of Nuclear Science **14**, 375(1964)

Sp78 D. A. Sparrow and A. S. Rosenthal, Physical Review **C18**, 1753(1978)

St81 A. Stetz, L. W. Swenson, J. Davis, J. Källne, R. C. Minehart, R. R. Whitney, V. Perez-Mendez, A. Sagle, J. Carroll, J. B. McClelland, and J. Faucett, Physical Review Letters **47**, 782(1981)

Su52 K.-H. Sun, F. A. Pecjak, and A. J. Allen, Physical Review **85**, 942(1952)

Ta65 Y. C. Tang and B. F. Bayman, Physical Review Letters **15**, 165(1965)

Te52 T. Teichman and E. P. Wigner, Physical Review **87**, 123(1952)

Th70 D. R. Thompson, Nuclear Physics **A143**, 304(1970)

TABLE 1

SPECTROMETER RELATIVE ACCEPTANCE

Table 1 gives the results of the spectrometer angular acceptance runs. The relative acceptance, defined as the true angular acceptance divided by the beam monitor efficiency, is displayed as a function of spectrometer $\frac{\Delta p}{p}$, the momentum range having been divided into 256 channels, each 0.2% wide.

TABLE 1

SPECTROMETER RELATIVE ACCEPTANCE

Channel	Acceptance (sr)	+/-
38.6	93.6	1.0
42.1	95.6	1.0
46.0	93.7	1.0
50.7	94.2	1.0
54.8	96.9	1.0
58.9	95.3	1.0
62.9	96.3	1.0
66.9	99.3	1.0
71.0	97.7	1.0
74.9	97.8	1.0
79.2	98.7	1.1
82.8	98.5	1.0
87.7	102.2	1.1
92.0	98.8	1.1
96.4	97.2	1.0
96.7	98.6	1.0
101.3	96.3	1.0
105.8	97.2	1.1
110.3	98.6	1.1
115.0	97.6	1.1
118.5	95.5	1.0
124.1	91.6	1.0
128.9	86.2	1.0
132.6	87.4	1.0
133.1	87.3	1.0
138.4	83.8	.9
143.0	80.7	.9
148.9	79.6	.9
153.8	79.1	.9
162.8	78.2	.9
168.6	76.0	.9

TABLE 2

CERENKOV DETECTOR EFFICIENCY

Table 2 lists the efficiency of the Cerenkov counter for detecting positrons as a function of spectrometer momentum channel. These figures were arrived at by the method described on page 24.

TABLE 2
CERENKOV DETECTOR EFFICIENCY

Channels	Efficiency (%)	+/-
1-51	92.6	.1
52-102	98.2	.3
103-154	98.1	.3
155-206	99.8	.1
207-255	98.2	.2

TABLE 3

WIRE CHAMBER EFFICIENCIES

Table 3 lists efficiencies of the 8 wire chamber planes as measured during a typical DCX run. Chamber 1 is the one furthest upstream, chamber 4 the furthest downstream. The x axis points in the direction of the spectrometer bend (vertical), while y is perpendicular to that.

TABLE 3
WIRE CHAMBER EFFICIENCIES

Plane	Efficiency (%)
1x	87.5
2x	99.0
3x	98.6
4x	97.0
1y	99.6
2y	99.9
3y	99.4
4y	83.9

TABLE 4

EXPERIMENTAL RESULTS

Table 4 lists the measured lab frame $\frac{d\sigma}{d\Omega dP}$ for the $^4He(\pi^-,\pi^+)4n$ reaction as a function of the outgoing π^+ momentum. The π^+ momentum has been corrected for energy loss in the target.

TABLE 4

EXPERIMENTAL RESULTS

Momentum (Mev/c)	$\frac{d\sigma}{d\Omega dP}$ (nb/(sr Mev/c))	+/-
211.1	87.5	7.
213.3	67.4	6.
215.5	68.5	6.
217.8	62.5	5.
220.0	61.4	5.
222.2	45.6	5.
224.5	44.5	5.
226.7	23.0	4.
228.9	17.8	3.
231.2	2.3	2.
233.4	0.0	2.
235.6	6.5	2.
237.9	8.9	2.
240.1	3.1	2.
242.3	2.7	1.
244.6	5.4	2.
246.8	2.9	1.
249.0	1.6	1.

TABLE 5

BEAM INTEGRATION $\pi \rightarrow \mu_{eff}$ SUMS

Table 5 lists the values and estimated errors of the accumulated $\pi \rightarrow \mu_{eff}$ (as defined on page 40) for the DCX and background runs.

TABLE 5

BEAM INTEGRATION $\pi \rightarrow \mu_{eff}$ SUMS

Runs	$\pi \rightarrow \mu_{eff}$	+/-
$^4He(\pi^-,\pi^+)4n$	111108024	95530
Background	95456032	105277

TABLE 6

PHASE SPACE FIT χ^2_ν

Table 6 lists the χ^2_ν values characterizing goodness of fit to the $^4He(\pi^-,\pi^+)4n$ $\frac{d\sigma}{d\Omega dP}$ data of curves corresponding to:

1) a pure 4 neutron phase space,

2) one pair of neutrons interacting in the $^1s_0$ state, and one pair noninteracting, and

3) two pairs of neutrons, each pair interacting in the $^1s_0$ state.

TABLE 6

PHASE SPACE FIT χ^2_ν

Final State	χ^2_ν (ν=10)
n+n+n+n	24.2
[2n]+n+n	14.9
[2n]+[2n]	4.2

FIGURE 1

FEYNMAN DIAGRAMS OF PROPOSED DCX REACTION MECHANISMS

Figure 1a depicts the conventional mechanism of DCX in which the incoming pion undergoes two successive single charge exchanges on nuclear protons.

Figure 1b is the diagram denoting the mechanism of Dalkarov *et al.*

Figure 1c represents the proposed scheme of Brown *et al.*

Figure 1d shows the diagram calculated by Germond and Wilkin.

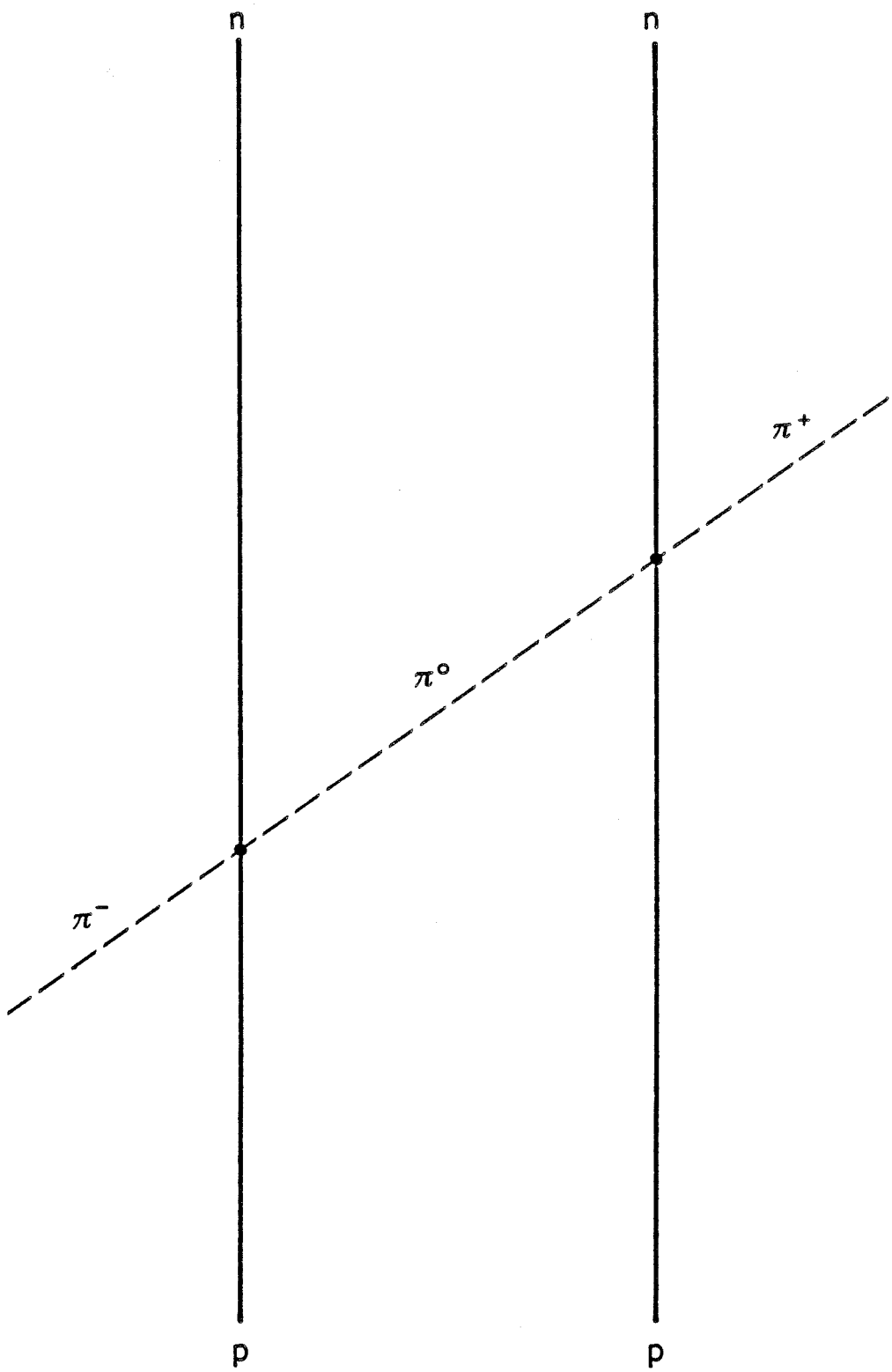
n
n
π^+
π°
π^-
p
p

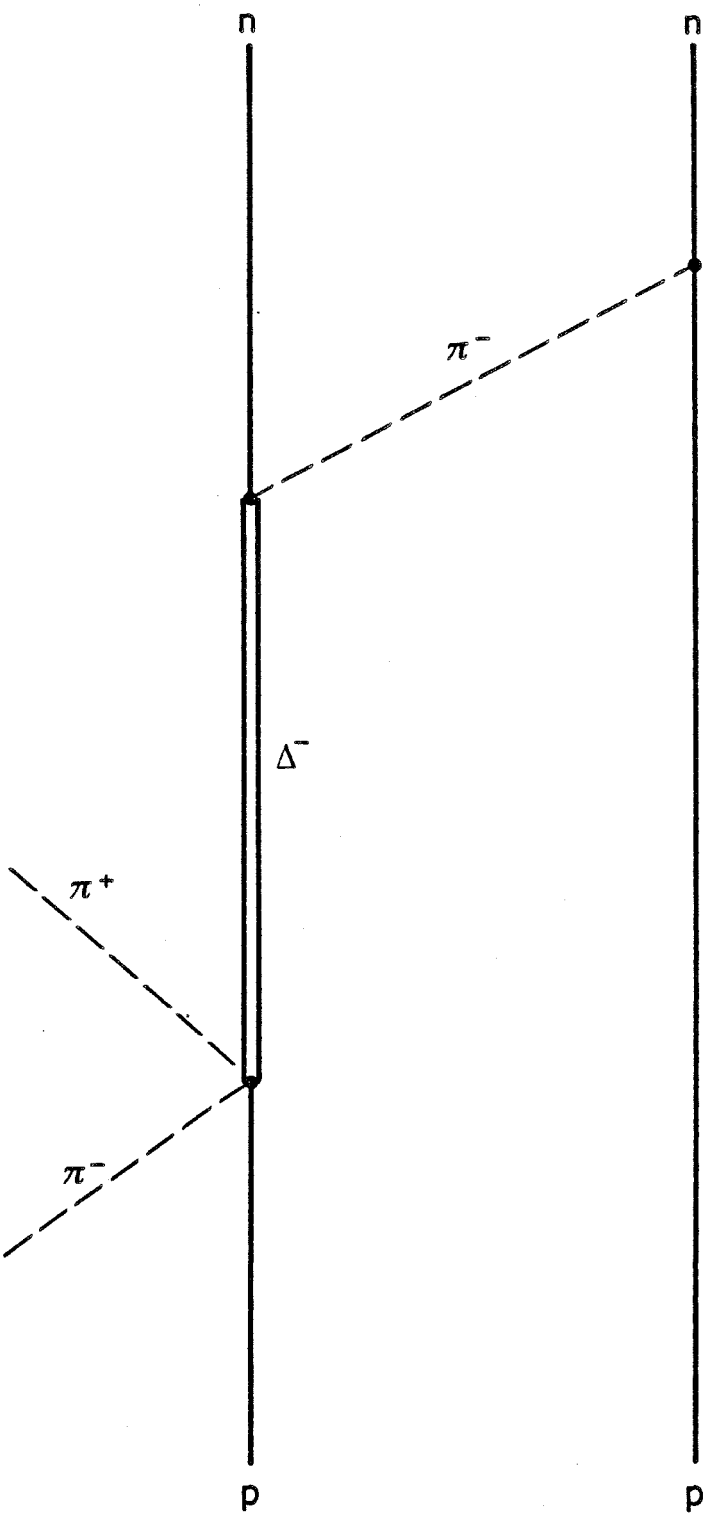
n
n
π^-
Δ^-
π^+
π^-
p
p

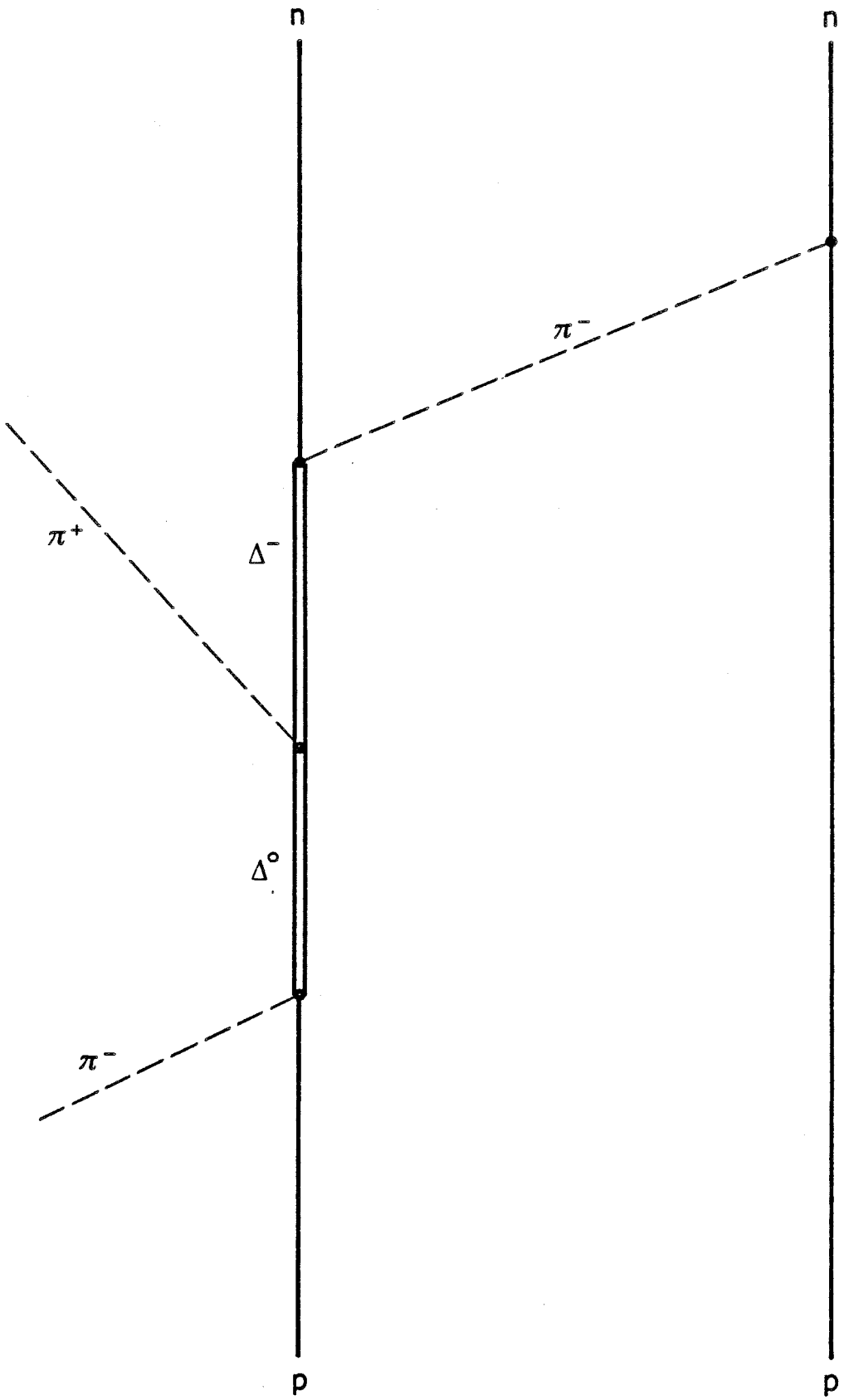
n
n
π^-
π^+
Δ^-
Δ°
π^-
p
p

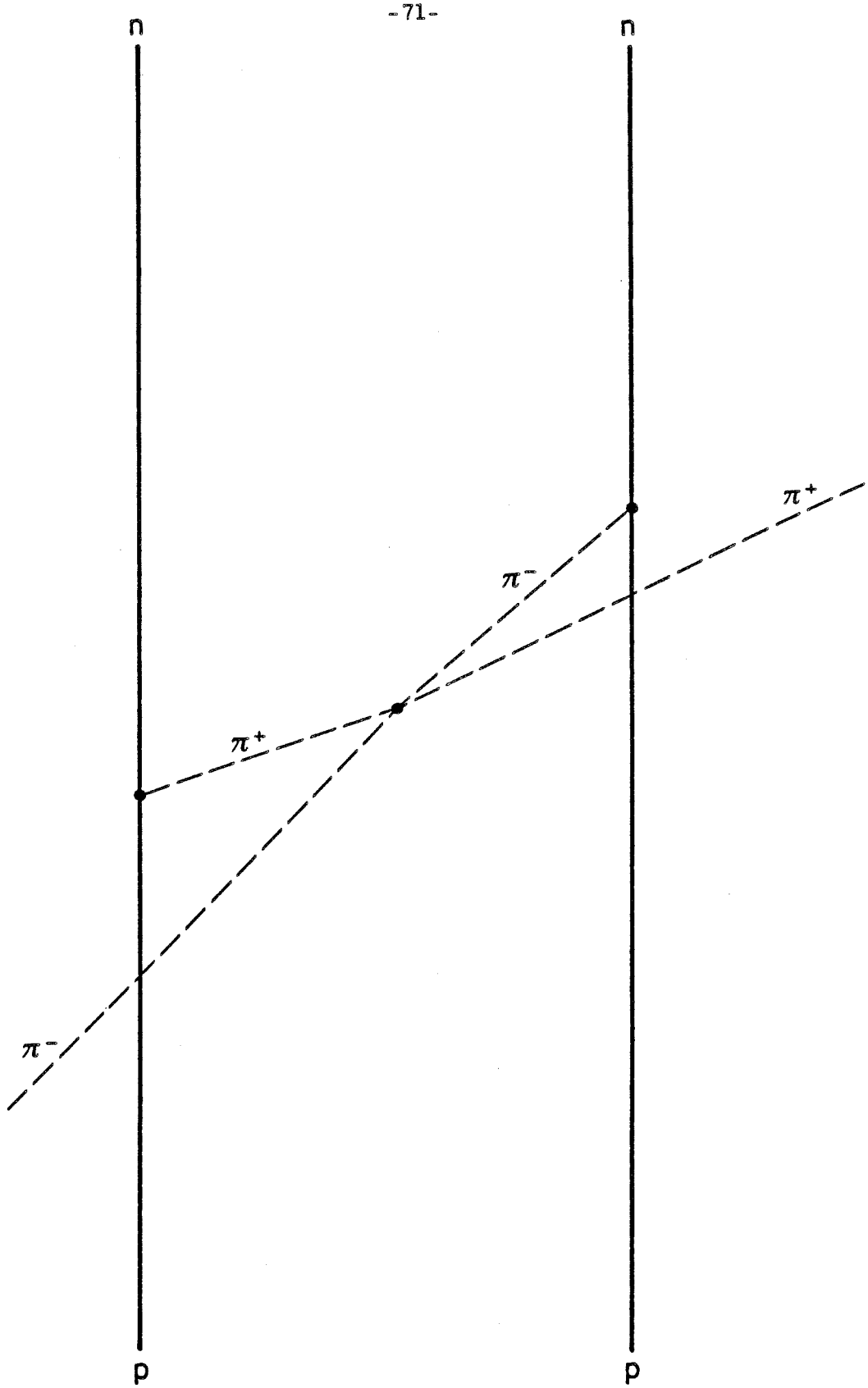
n
n
π^+
π^-
π^+
π^-
p
p

FIGURE 2

PREVIOUS MEASUREMENTS AND CALCULATIONS OF $^4He(\pi^+,\pi^-)4p$

Figure 2, from Stetz *et al*, shows measured and calculated total cross sections for the $^4He(\pi^+,\pi^-)4p$ reaction as a function of the π^+ bombarding energy. The hatched area between the curves labeled 1 corresponds to the results of the pair mechanism calculation of Becker and Schmit, while the curves labeled 3 and 3' are the similar calculations of Gibbs *et al*, neglecting and including Pauli principle effects, respectively. Curve number 2 is the prediction of Germond and Wilkin using the virtual pion scattering mechanism.

The solid data points are the measurements of Falomkin *et al*, the open point is that reported by Carayannopoulos *et al*, and the crosses are due to Stetz *et al*.

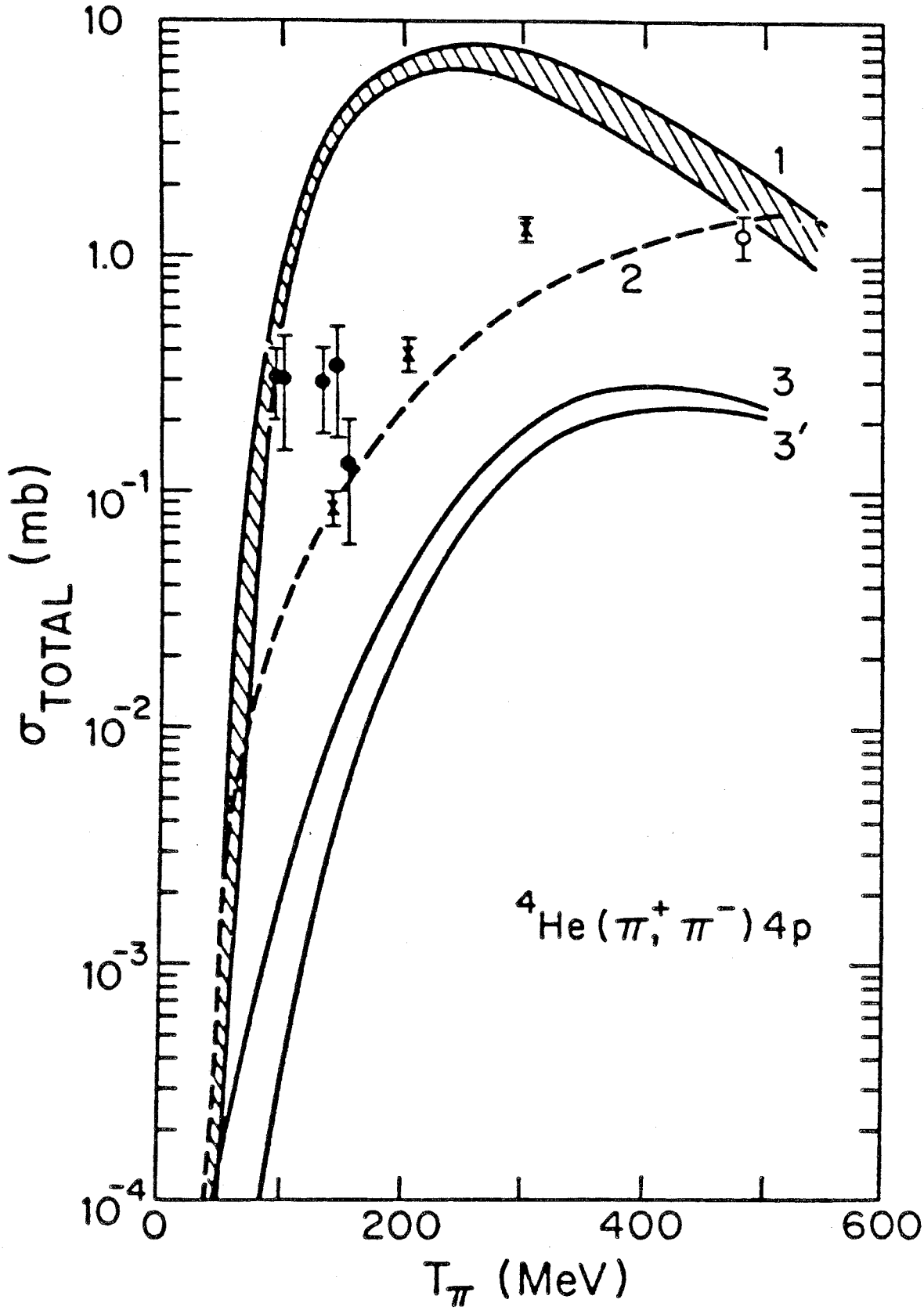
10
1.0
10^{-1}
10^{-2}
10^{-3}
10^{-4}
σ_{TOTAL} (mb)
0
200
400
600
T_π (MeV)
1
2
3
3'
$^4He(\pi^+,\pi^-)4p$

FIGURE 3

EXPERIMENTAL CONFIGURATION

Figure 3 is a schematic overview of the experimental setup.

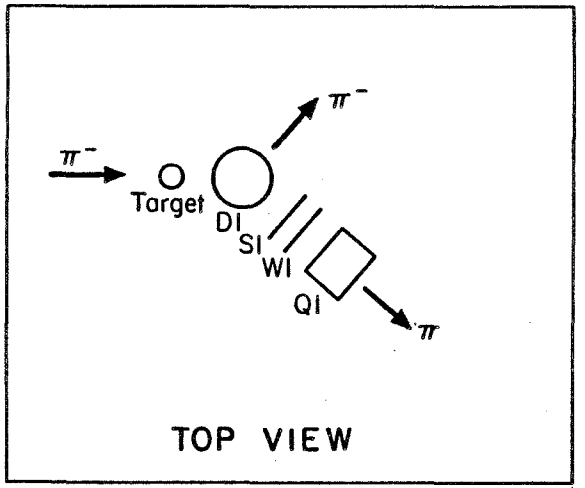
π⁻
Target
D1
S1
W1
Q1
π⁻
π
TOP VIEW

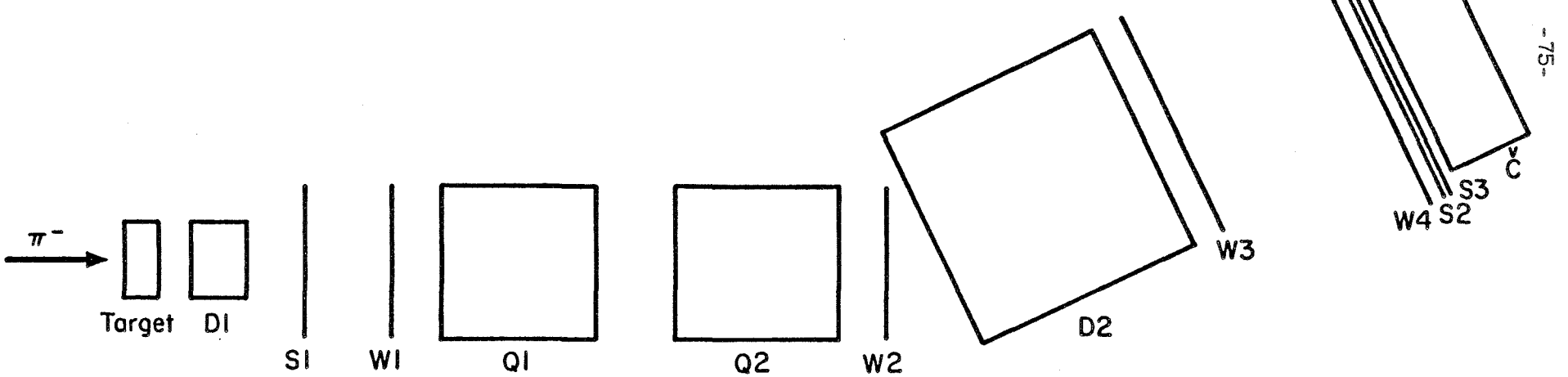
π⁻
Target
D1
S1
W1
Q1
Q2
W2
D2
W3
W4
S2
S3
C

SIDE VIEW

FIGURE 4

^{4}He TARGET SYSTEM

Figure 4 details the cryogenic ^{4}He target system as designed by Meyer (Me74).

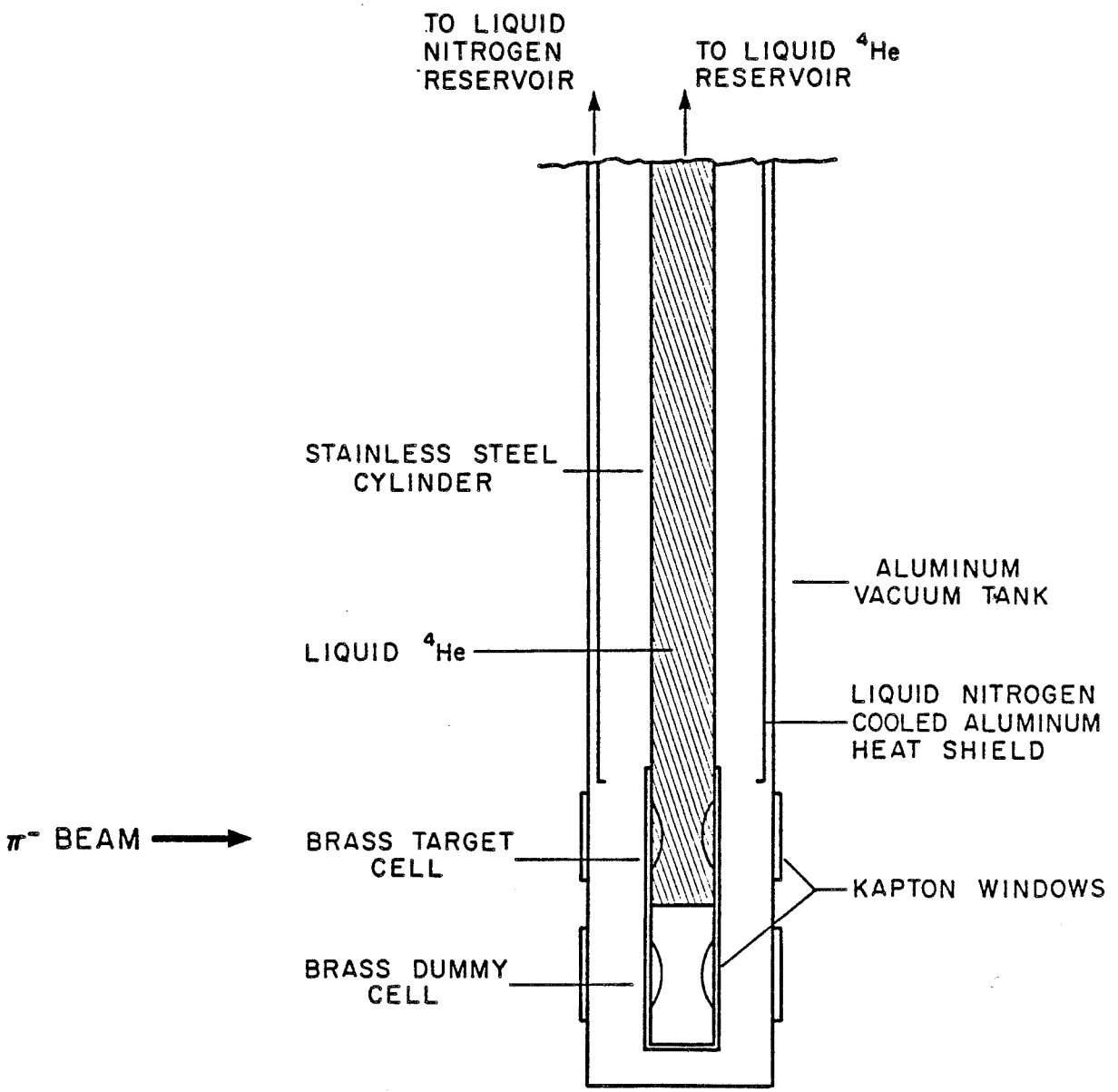
TO LIQUID NITROGEN RESERVOIR
TO LIQUID ^{4}He RESERVOIR
STAINLESS STEEL CYLINDER
ALUMINUM VACUUM TANK
LIQUID ^{4}He
LIQUID NITROGEN COOLED ALUMINUM HEAT SHIELD
π^- BEAM
BRASS TARGET CELL
KAPTON WINDOWS
BRASS DUMMY CELL

FIGURE 5

CERENKOV COUNTER

Figure 5 shows construction details of the Cerenkov counter.

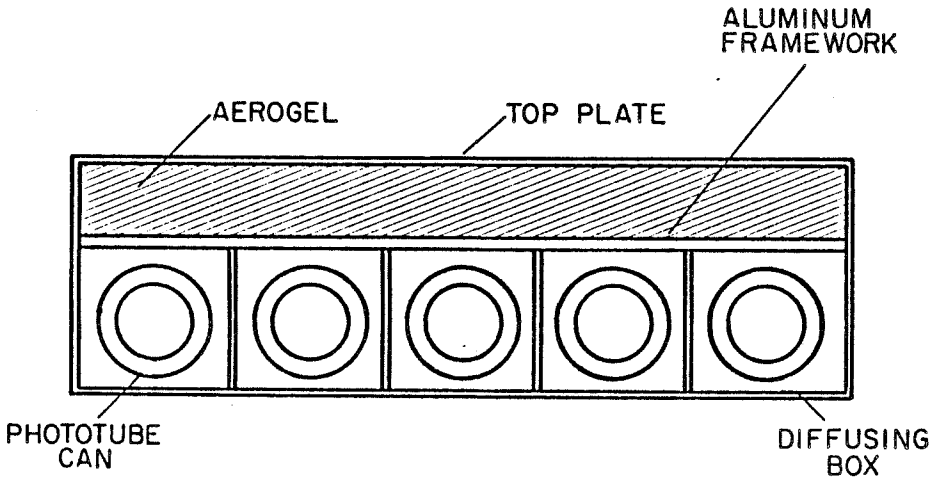

SIDE VIEW

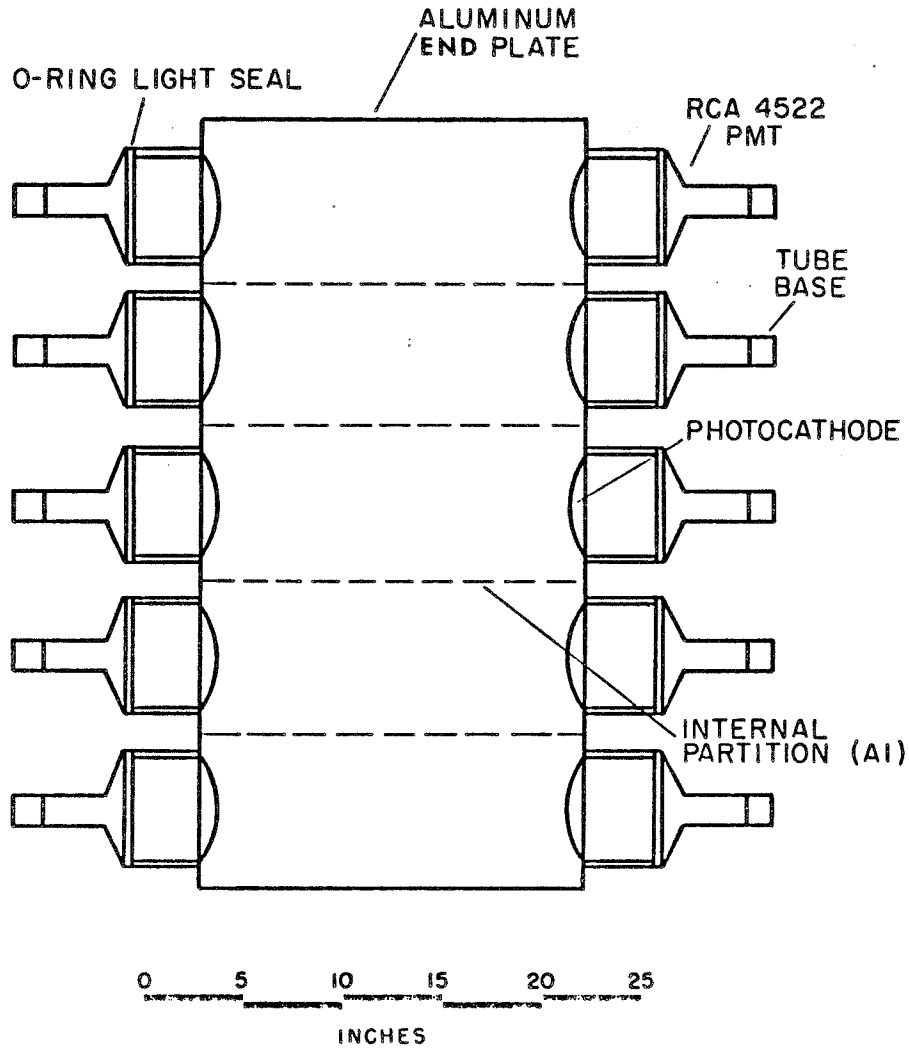

TOP VIEW

FIGURE 6

BEAM INTEGRATION MONITOR

Figure 6 shows the arrangement of plastic scintillators and electronics used to monitor the bombarding π^+ beam flux. Rectangles labeled D are discriminators, those labeled C are coincidence boxes.

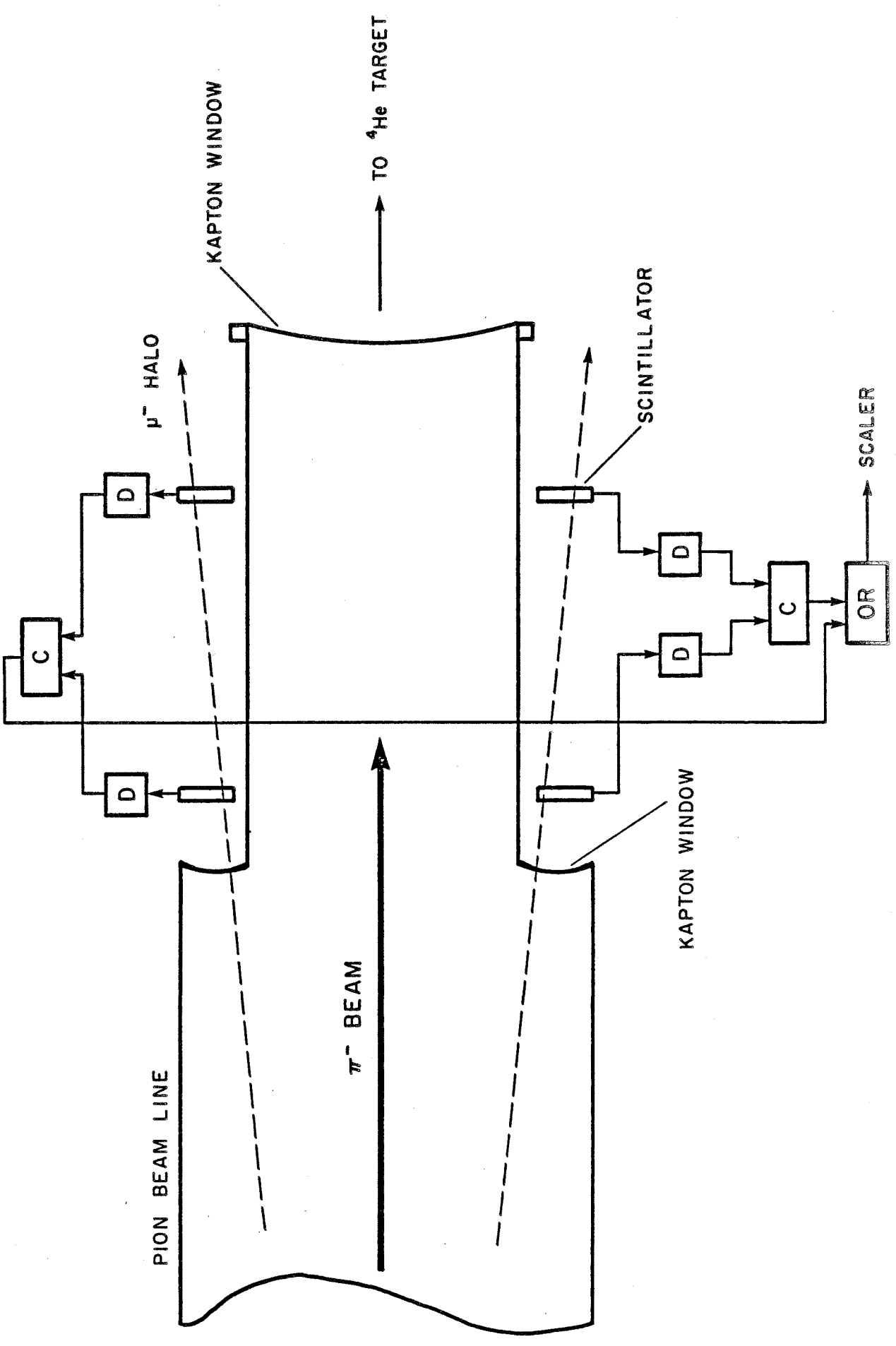
TO ^{4}He TARGET
KAPTON WINDOW
μ^- HALO
SCINTILLATOR
SCALER
D
D
C
D
D
C
OR
KAPTON WINDOW
π^- BEAM
PION BEAM LINE

FIGURE 7

ELECTRONICS

Figure 7a is a simplified diagram of the data acquistion logic. For the sake of clarity, discriminators, amplifiers, and fanouts have been deleted. The two dotted lines at the top of the figure lead to figure 7b, where the modifications introduced to reduce dead time and magnetic tape consumption are shown.

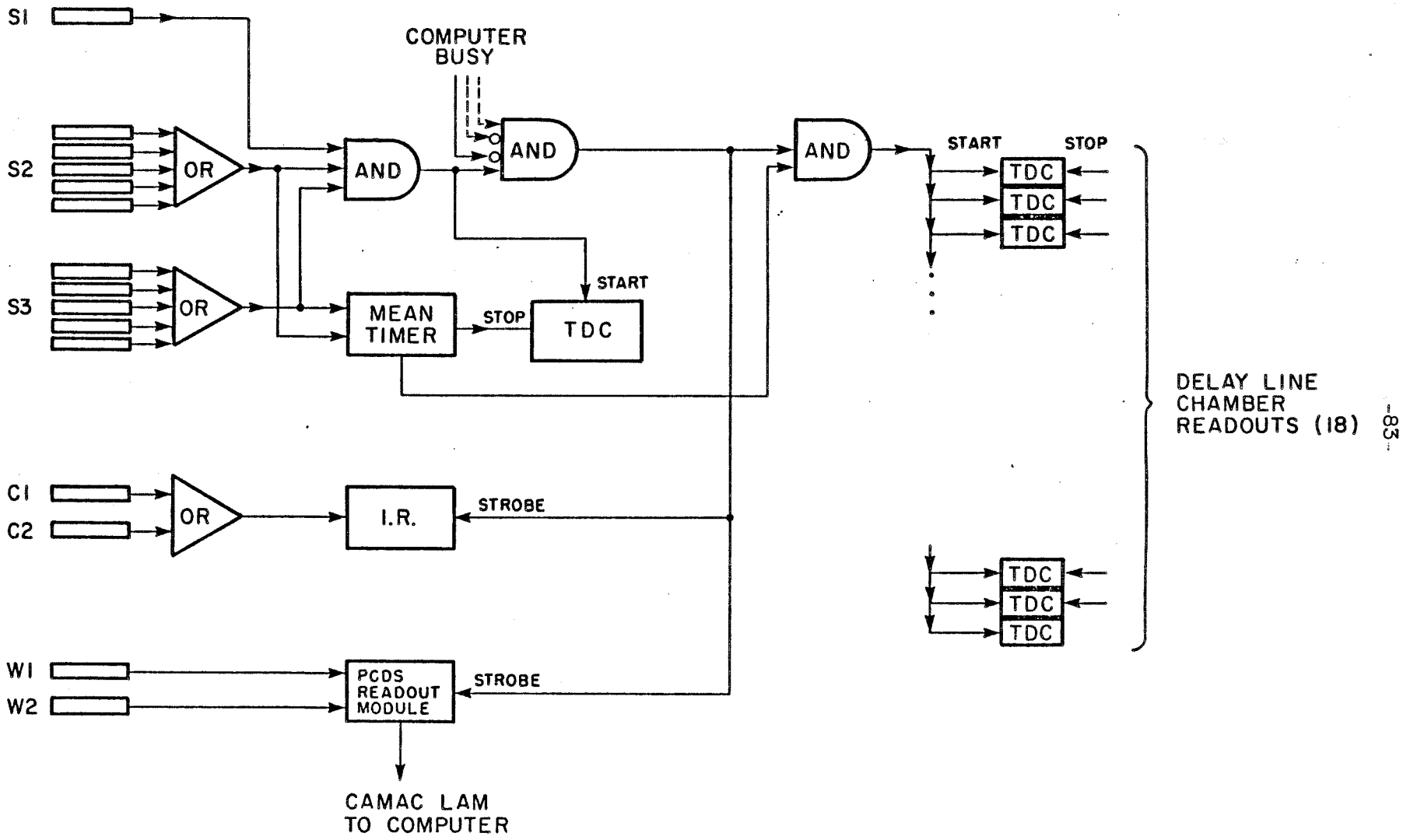
S1
S2
S3
OR
OR
COMPUTER
BUSY
AND
AND
AND
START
STOP
MEAN
TIMER
STOP
TDC
START
TDC
TDC
TDC
C1
C2
OR
I.R.
STROBE
TDC
TDC
TDC
W1
W2
PCDS
READOUT
MODULE
STROBE
CAMAC LAM
TO COMPUTER
DELAY LINE
CHAMBER
READOUTS (18)

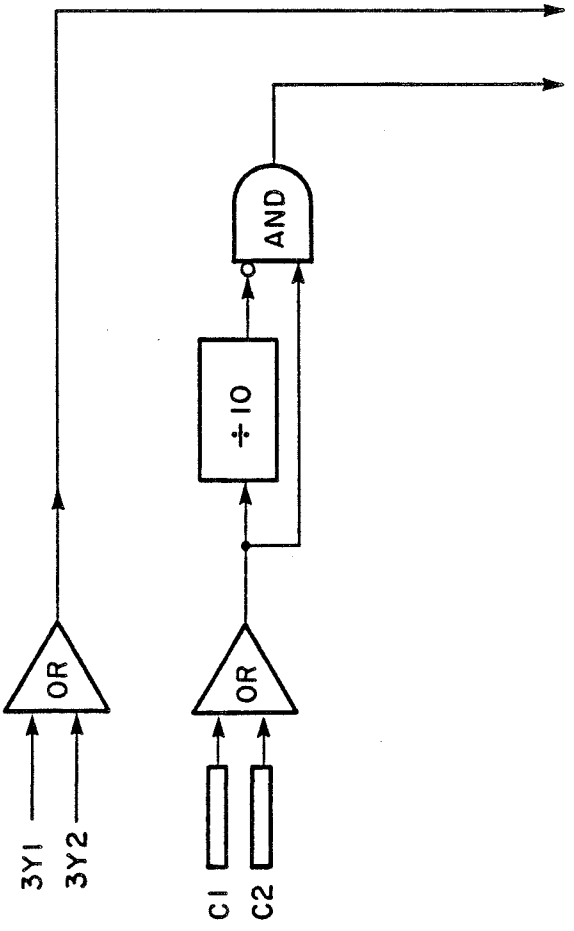
AND
÷10
OR
OR
3Y1
3Y2
C1
C2

FIGURE 8

PROTON MOMENTUM SPECTRUM

Figure 8 is the momentum spectrum of recoil protons from the 180° elastic scattering of π^- on a CH_2 during a typical acceptance run. The broad background below the elastic peak is due to Fermi broadened quasielastic protons from the ^{12}C.

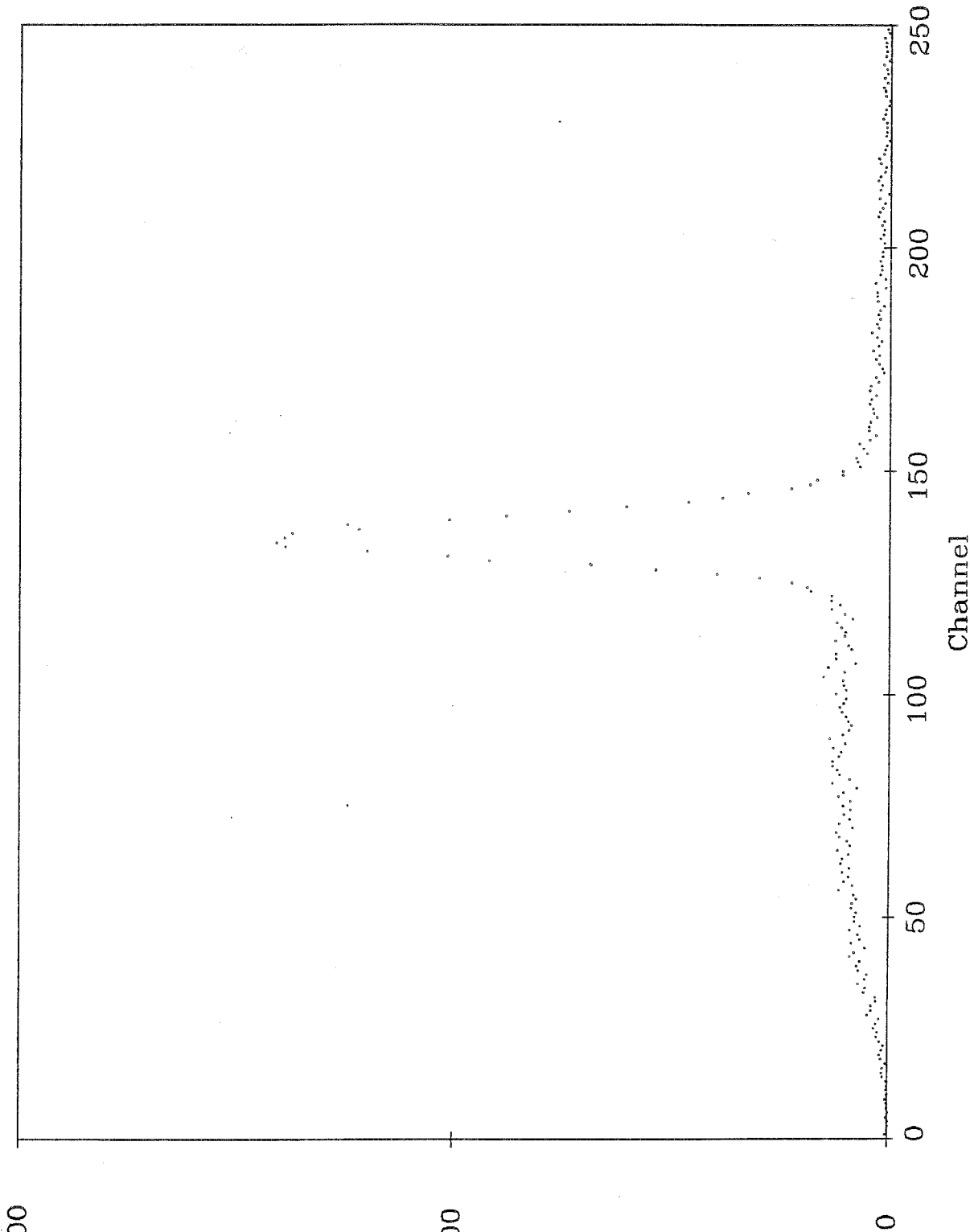
1000
500
0
Counts
0
50
100
150
200
250
Channel

FIGURE 9

RELATIVE ACCEPTANCE PLOT

Figure 9 plots the relative acceptance of the spectrometer, defined as the true angular acceptance divided by the beam monitor efficiency. These data are tabulated in table 1.

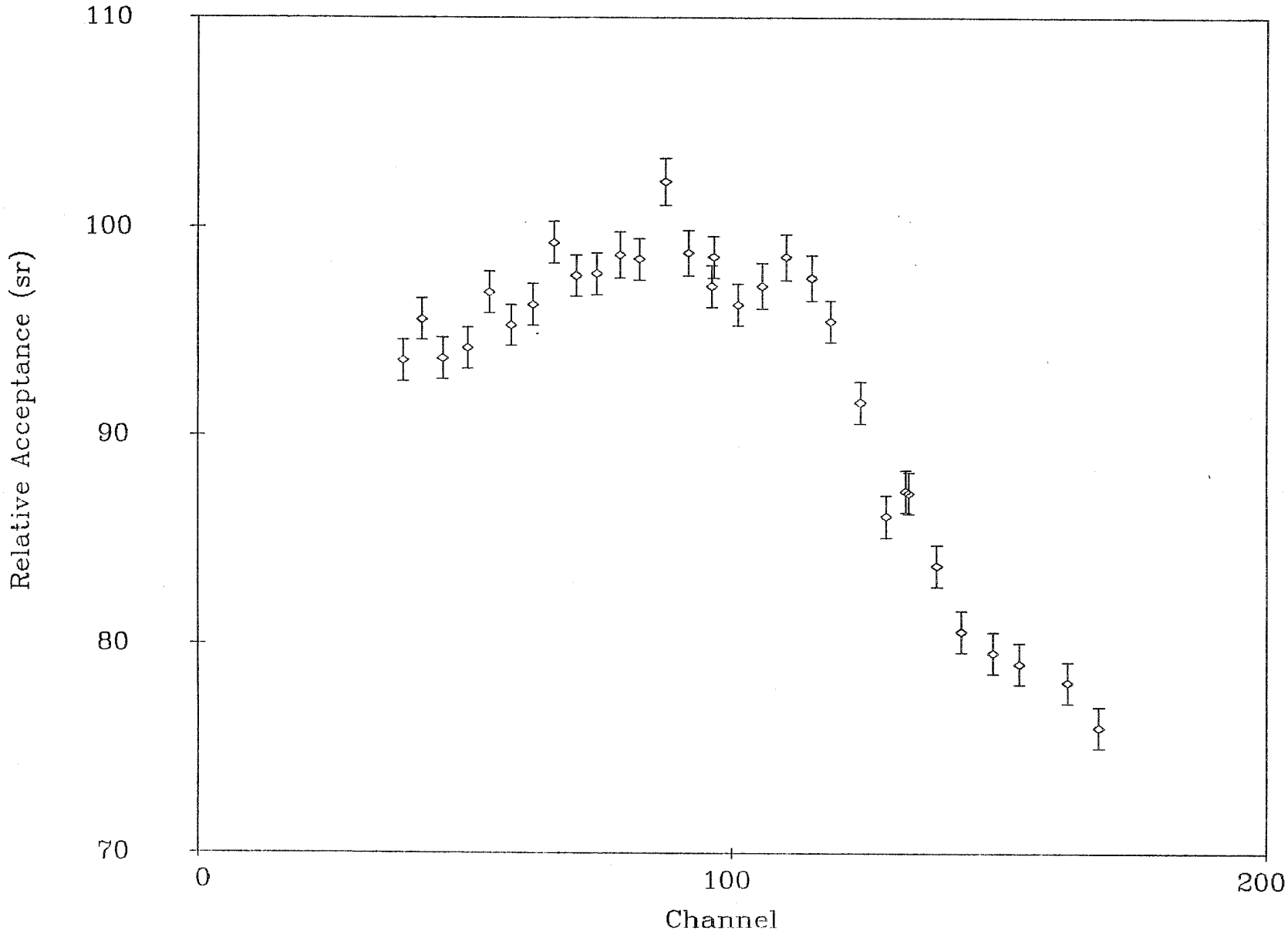
110
100
90
80
70
Relative Acceptance (sr)
0
100
200
Channel

FIGURE 10

$^{12}C(\pi^-,\pi^+)^{12}Be$ DIFFERENTIAL CROSS SECTION

Figure 10 shows $\frac{d\sigma}{d\Omega dP}$(lab) for the reaction $^{12}C(\pi^-,\pi^+)^{12}Be$ measured at 8°, with an incident π^- kinetic energy of 165 Mev. The peak is primarily due to the three lowest lying states of ^{12}Be.

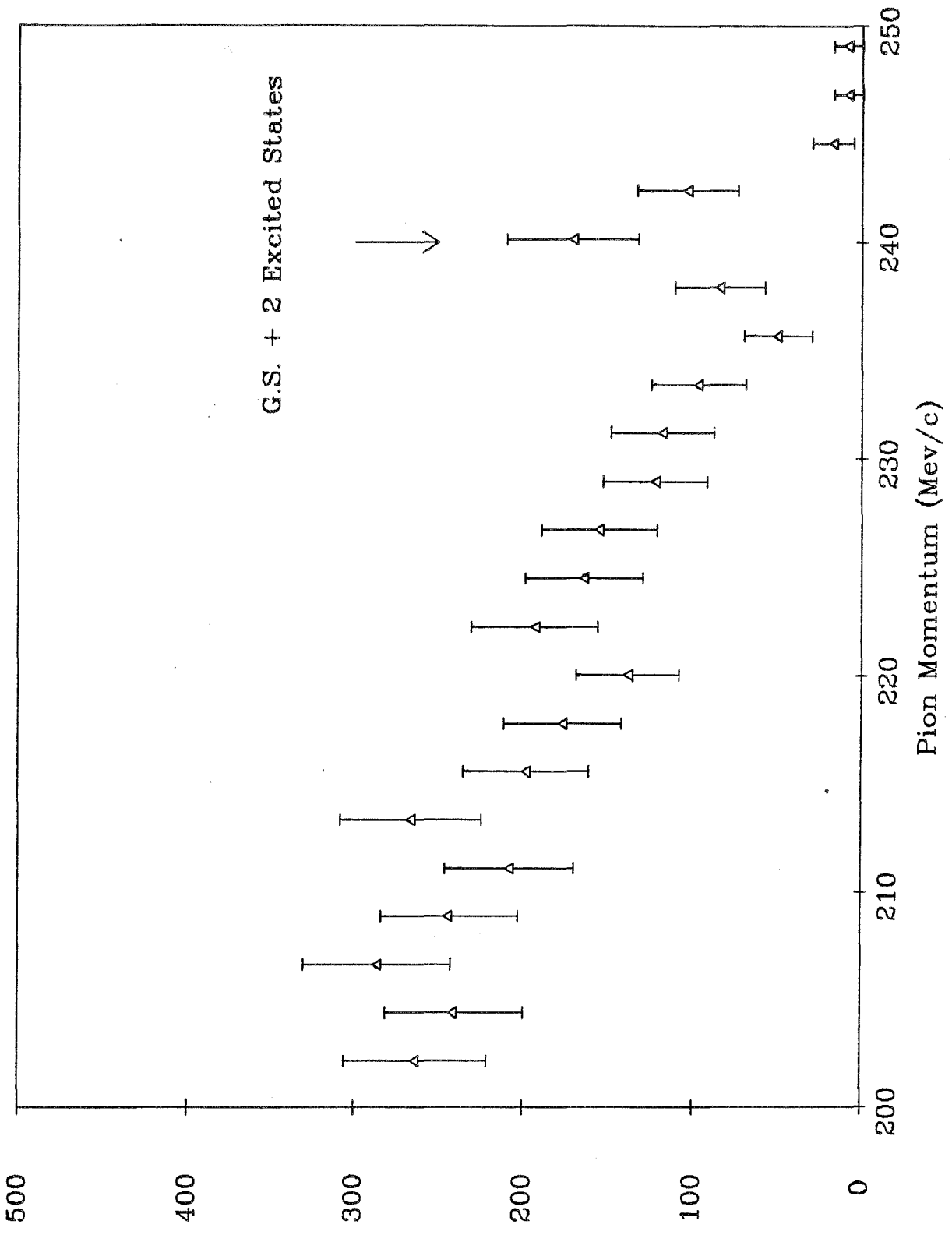
G.S. + 2 Excited States
Differential Cross Section (nb/(sr Mev/c))
Pion Momentum (Mev/c)
0
100
200
300
400
500
200
210
220
230
240
250

FIGURE 11

TIME OF FLIGHT SPECTRUM

Figure 11 shows the time of flight between S1 and S2-S3 of particles passing through the spectrometer as recorded during a typical Helium DCX run, each channel being 200 ps wide. Figure 11a is the spectrum of events in anticoincidence with the Cerenkov pulses, while 11b was taken in coincidence. Due to the electronics modification shown in figure 7b, figure 11b shows only 10% of the actual number of particles that triggered the spectrometer.

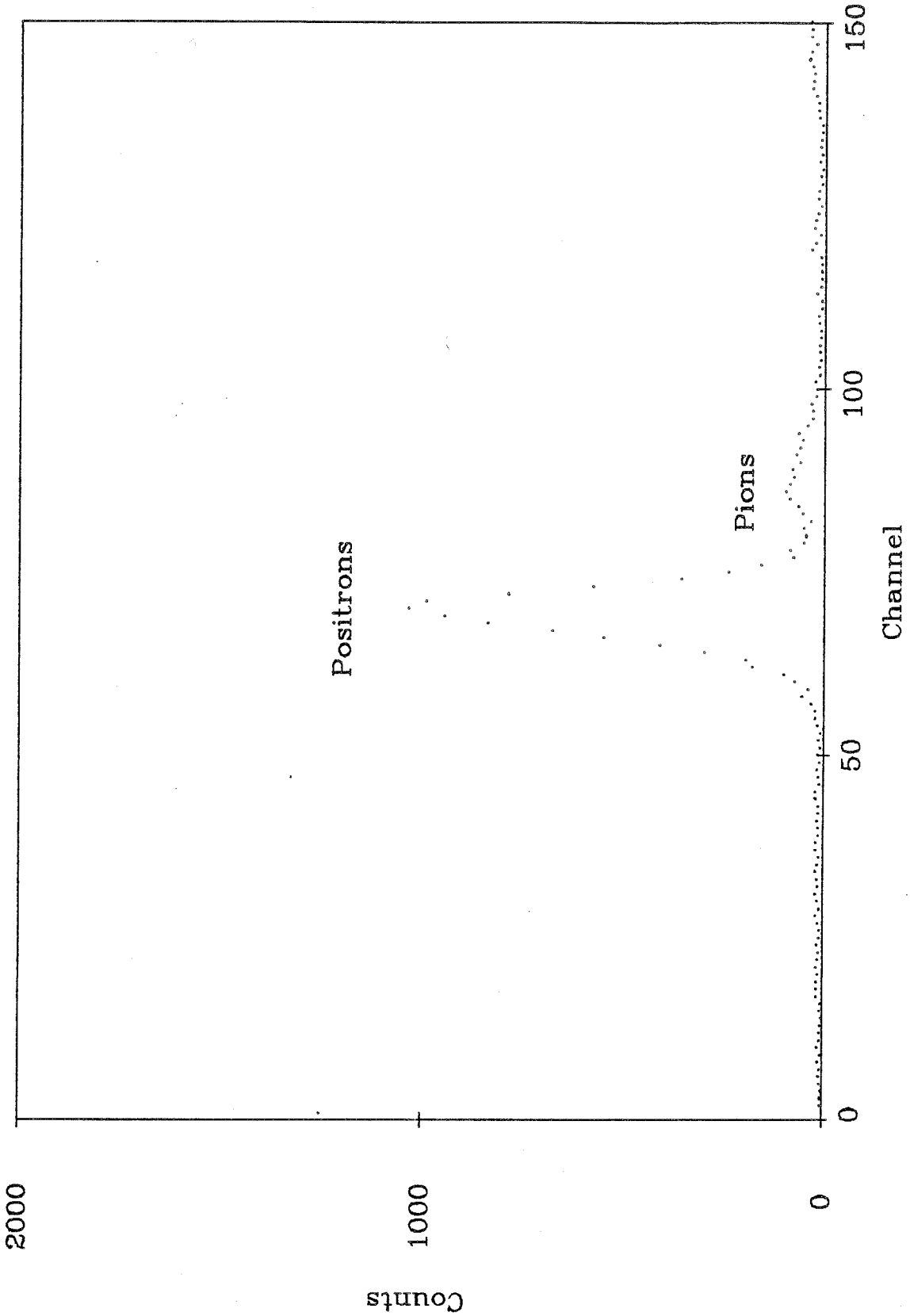
Positrons
Pions
Counts
Channel
2000
1000
0
0
50
100
150

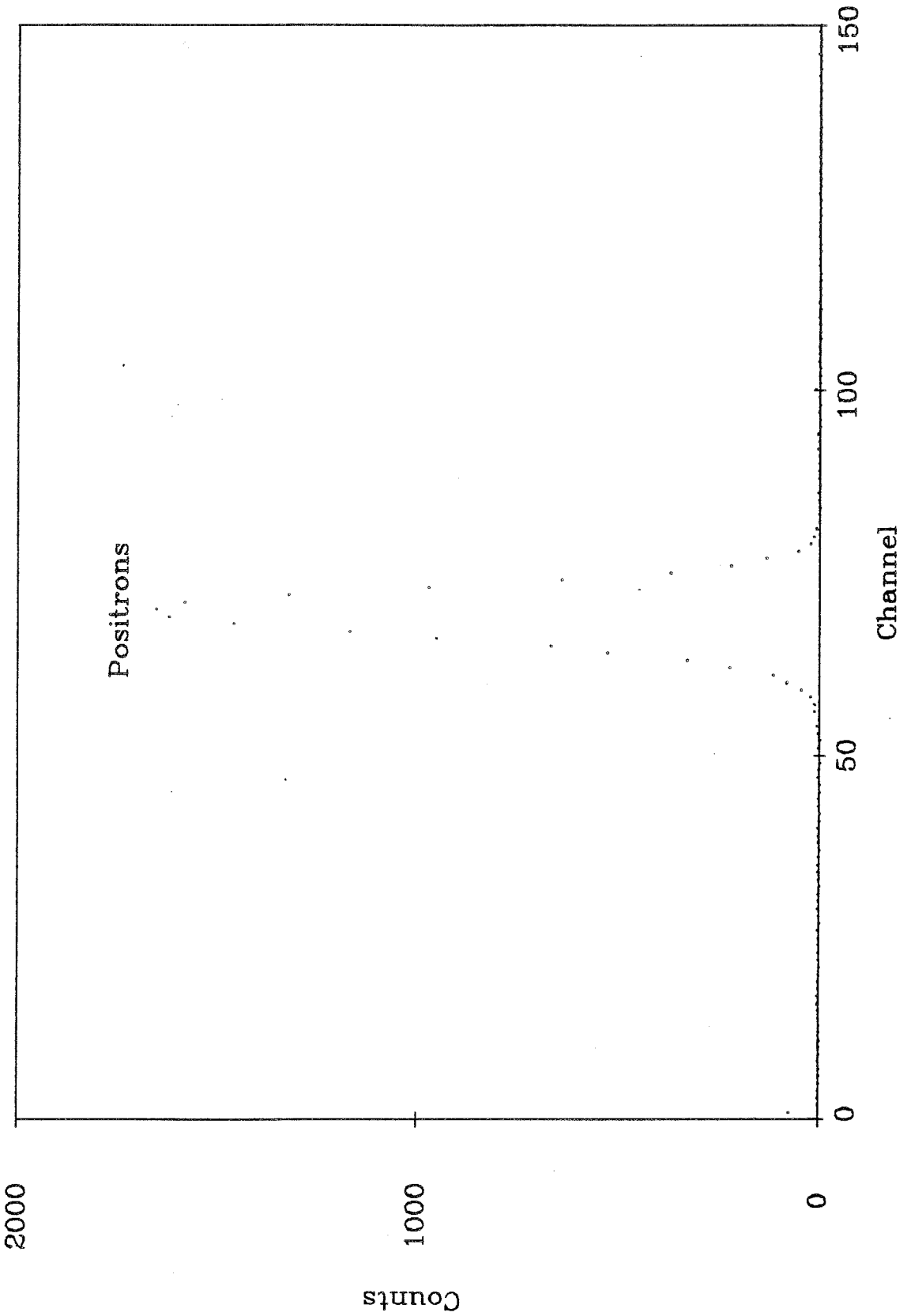
Positrons
Counts
2000
1000
0
0
50
100
150
Channel

FIGURE 12

GOODNESS OF FIT DISTRIBUTION

Figure 12 shows the distribution of "goodness of fit" values (as defined on page 37) of all events processed by the software during a typical Helium DCX run. The muon rejection cut was taken at channel 76.

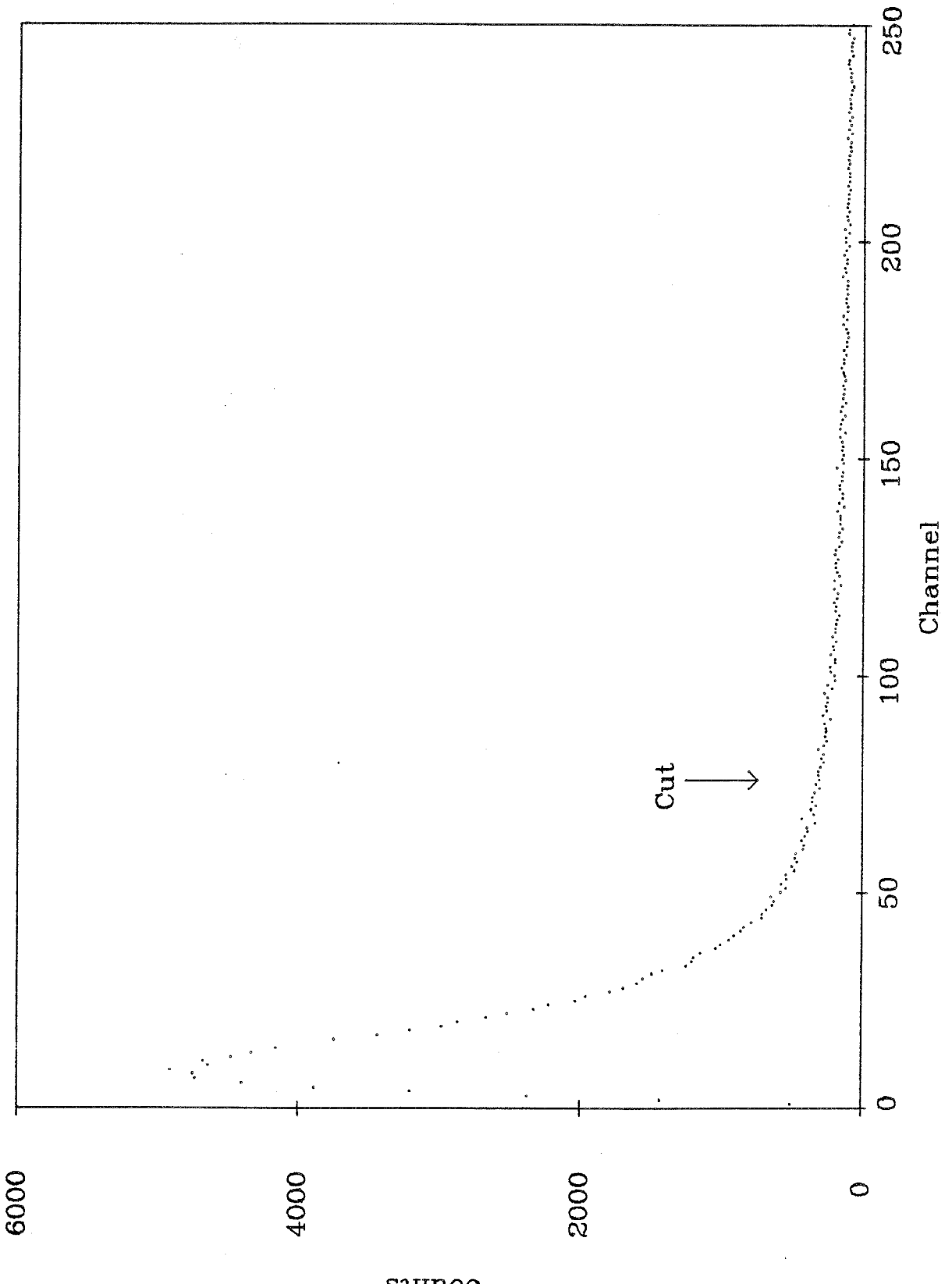
Counts
6000
4000
2000
0
0
50
100
150
200
250
Channel
Cut

FIGURE 13

BACKGROUND SPECTRUM

Figure 13 shows the π^+ momentum spectrum obtained with the background cell, analyzed identically to the Helium runs, and displayed with the same scale as figure 14. The curve drawn through the curves is the fitted function used for the actual background subtraction.

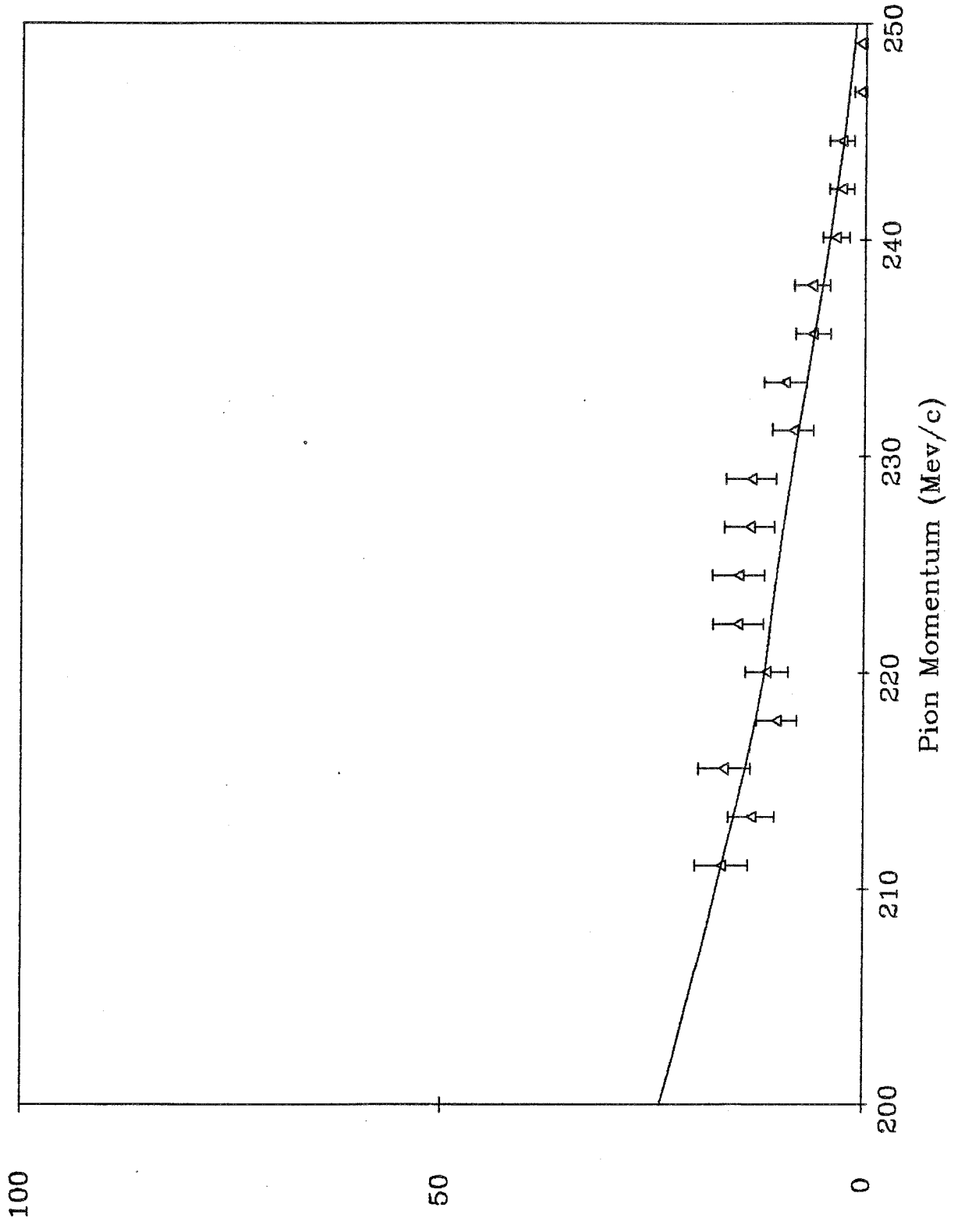
Differential Cross Section (nb/(sr Mev/c))
100
50
0
200
210
220
230
240
250
Pion Momentum (Mev/c)

FIGURE 14

EXPERIMENTAL RESULTS

$\frac{d\sigma}{d\Omega dP}$ (lab frame) is plotted against the π^+ momentum. Energy loss of pions in the target has been corrected for, and the background spectrum of figure 13 has been subtracted. The two arrows correspond to a binding of the four neutron final state by 0 and 3.1 Mev, as indicated.

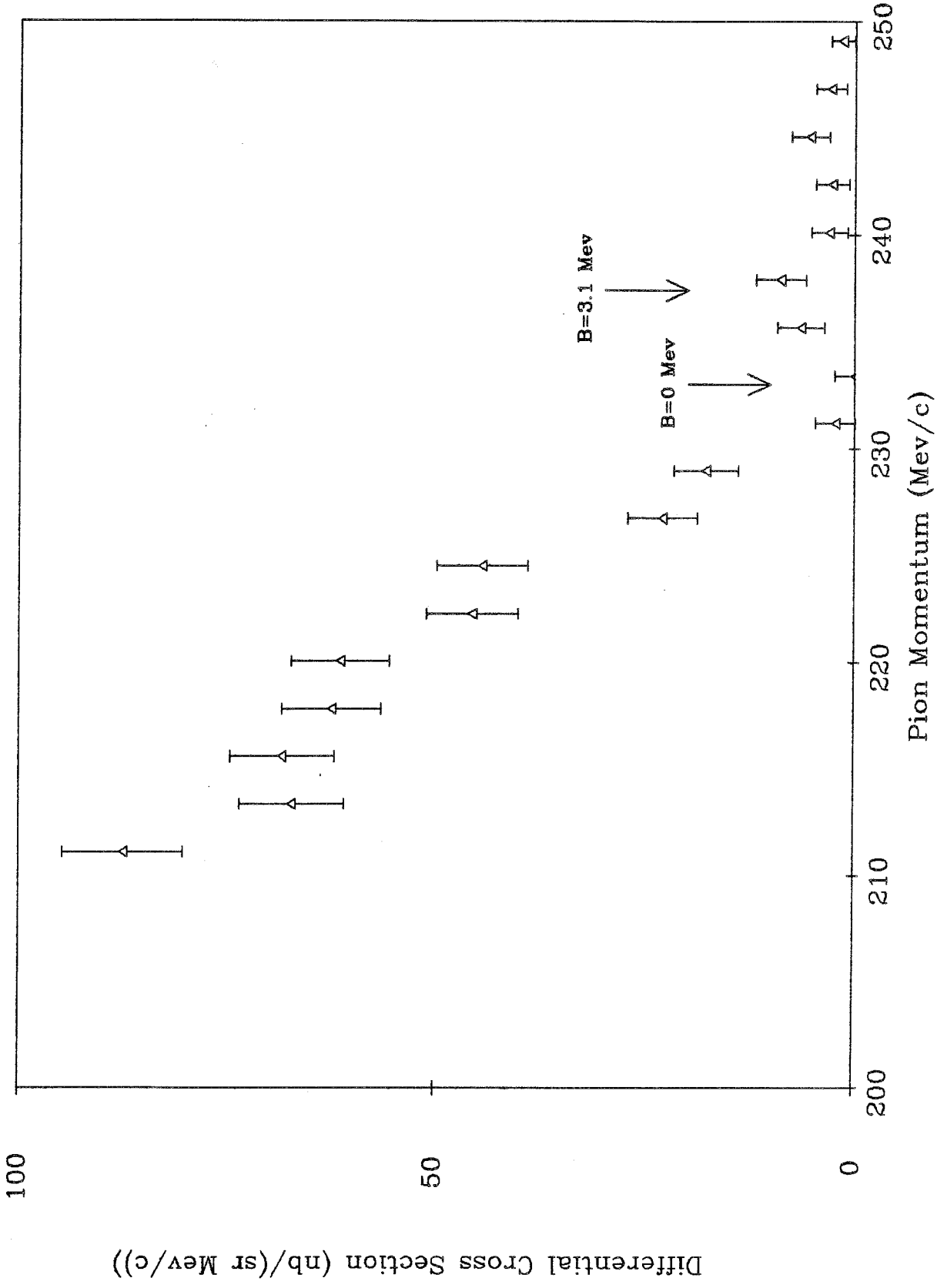
Differential Cross Section (nb/(sr Mev/c))
100
50
0
200
210
220
230
240
250
Pion Momentum (Mev/c)
B=0 Mev
B=3.1 Mev

FIGURE 15

PREVIOUS MEASUREMENT OF $^4He(\pi^-,\pi^+)4n$

Figure 15 shows the results of the Kaufman *et al* measurement of $^4He(\pi^-,\pi^+)4n$ at T_{π^-} = 140 Mev.

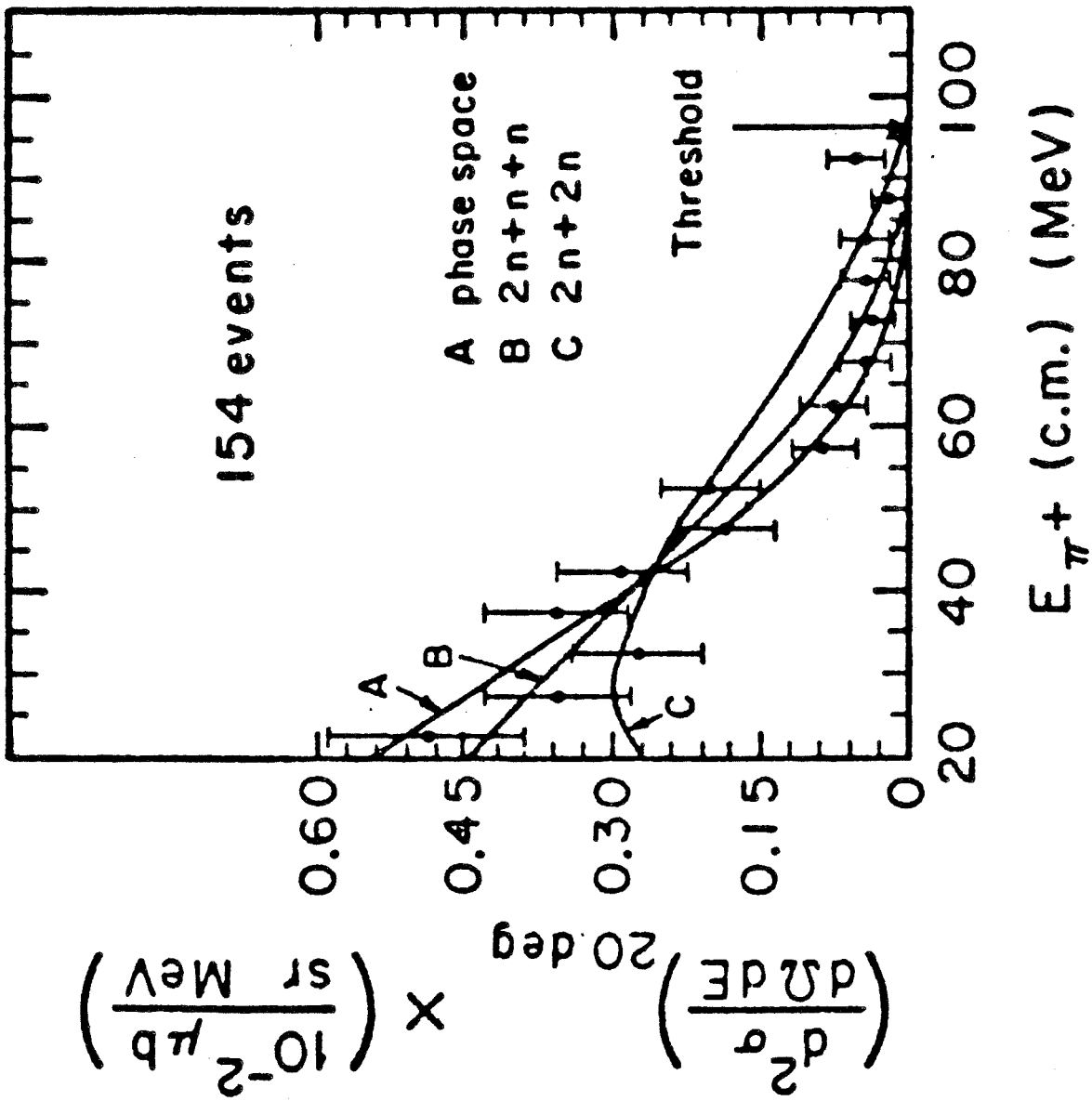
154 events
A phase space
B 2n+n+n
C 2n+2n
Threshold
A
B
C
0.60
0.45
0.30
0.15
0
20
40
60
80
100
E_{π^+} (c.m.) (MeV)
$\left(\frac{d^2\sigma}{d\Omega\, dE}\right)_{20\,deg}$
$\times \left(\frac{10^{-2}\ \mu b}{sr\ MeV}\right)$

FIGURE 16

COMPARISON OF PRESENT RESULTS WITH PHASE SPACE CURVES

Figure 16 displays the data of figure 14 as compared to "best fit" curves corresponding to pure 4 neutron phase space (solid curve), one pair of neutrons interacting in the $^1s_0$ state, with the other pair noninteracting (dot-dashed curve), and two $^1s_0$ neutron pairs (dotted curve).

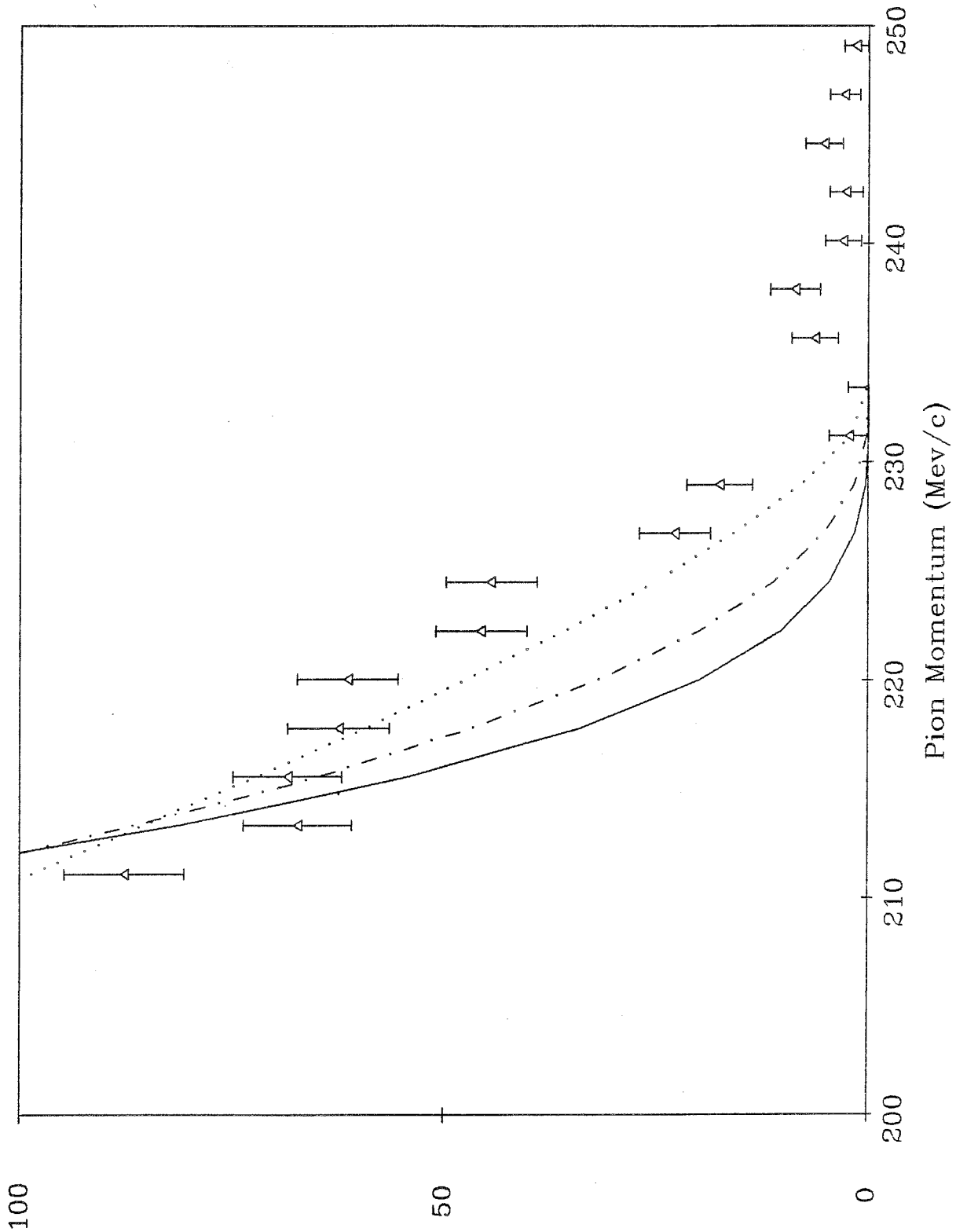
Differential Cross Section (nb/(sr Mev/c))
100
50
0
200
210
220
230
240
250
Pion Momentum (Mev/c)